https://doi.org/10.5194/egusphere-2026-1686
Preprint. Discussion started: 10 April 2026

Airborne performance assessment of the DLR MIRO MGA^3 quantum cascade laser spectrometer for fast N_2O measurements

Leon Knez[1], Maximilian Eckl[a,b], Paul Waldmann[1], Alina Fiehn[1], Magdalena Pühl[1], Oleg Aseev[2], Glenn S. Diskin[3], Joshua P. DiGangi[3], Yonghoon Choi[3,4], Jason A. Miech[3,5], Ryan Bennett[6,7], Charles K. Gatebe[6], Jonathan M. Dean-Day[6,8], Rajesh Poudyal[6,8], Gangwoong Lee[9], Jeonghwan Kim[9], and Anke Roiger[1]

[1]Institut für Physik der Atmosphäre, Deutsches Zentrum für Luft- und Raumfahrt e.V. (DLR), 82234 Wessling, Germany
[2]MIRO Analytical AG, Wallisellen, Switzerland
[3]NASA Langley Research Center, Hampton, VA, USA
[4]Analytical Mechanics Associates, Hampton, VA, USA
[5]Oak Ridge Associated Universities, Oak Ridge, TN, USA
[6]NASA Ames Research Center, Moffett Field, CA, USA
[7]National Suborbital Research Center, Grand Forks, ND, USA
[8]Bay Area Environmental Research Institute, Moffett Field, CA, USA
[9]Hankuk University of Foreign Studies, Seoul, Republic of South Korea
[a]formerly at: Institut für Physik der Atmosphäre, Deutsches Zentrum für Luft- und Raumfahrt e.V. (DLR), 82234 Wessling, Germany
[b]now at: E.ON Energy Markets GmbH, Essen, Germany

Correspondence: Leon Knez (leon.knez@dlr.de)

Abstract.

Nitrous oxide (N_2O) is the most dominant precursor of ozone-depleting substances and the third most important anthropogenic greenhouse gas, with agriculture contributing the largest share of emissions (56%). Over the past two decades, airborne in-situ measurements have become increasingly important for studying emission and transport of N2O in the atmosphere, also driven by the development of more precise and simultaneously faster Quantum Cascade Laser (QCL)-based spectrometers.

However, many QCL-based spectrometers exhibit sensitivities to environmental and flight-related parameters that can vary rapidly ($\leq 1\,\mathrm{s}$), such as static or cabin pressure and aircraft roll and pitch angles. The impact of changing ambient water vapor is particularly critical due to both dilution and quantum-mechanical effects. Because the variability of N_2O in the lower troposphere is often very small (<$1\,\mathrm{ppb}$) relative to its high background ($\sim 338\mathrm{ppb}$), even minor variations in these parameters can significantly affect data quality and must be corrected. Although many instruments can resolve such small concentration changes, their typical temporal resolution of $1\,\mathrm{Hz}$ may limit the application of advanced measurement techniques such as eddy covariance on fast-moving aircraft.

Here, we present and evaluate a new instrument setup for precise ($< 0.2\,\mathrm{ppb}$) and high-frequency ($10\,\mathrm{Hz}$) airborne in-situ N_2O measurements in altitudes up to $4500\,\mathrm{m}$ based on a MIRO MGA^3 QCL spectrometer (MIRO Analytical AG). The instrument was successfully deployed during two airborne science missions, namely onboard the unpressurized DLR Cessna during the Greenhouse Gas Monitoring (GHGMon) campaign in 2023 in the Netherlands, as well as onboard the NASA

https://doi.org/10.5194/egusphere-2026-1686
Preprint. Discussion started: 10 April 2026

DC8 during the Satellite Investigation of the Asian Air Quality (ASIA-AQ) campaign in 2024. Specifically, we evaluate and compare different water vapor correction approaches using ASIA-AQ data sampled within the tropical boundary layer over South Korea, the Philippines, Thailand and Taiwan, which partly were characterized by specifically high ambient humidity (up to 30000 ppm H_2O). The water vapor correction methods include an empirical approach that relies on both native and corrected MIRO in-flight water vapor measurements, as well as an approach by an updated version of the MIRO specific fitting software. Comparison with N_2O measurements from a well-established instrument onboard the NASA DC8 shows agreement within combined measurement uncertainties for all tested water vapor correction approaches, albeit special caution is needed for humidities larger than 15000 ppm. The new water vapor corrected data shows a 42 % better precision than with original default settings of the instrument. We further show that the instrument setup is insensitive to flight parameter changes such as roll and pitch angle of the aircraft, and allows for stable measurements even under challenging conditions such as in the turbulent boundary layer.

This instrument setup enables improved characterization of N_2O emissions and sources from the agricultural sector which is, in particular, relevant for tropical regions with strong agricultural activity and high humidity, where observational data remain scarce.

1 Introduction

Nitrous Oxide (N_2O) is, after carbon dioxide (CO_2) and methane (CH_4), the third most important anthropogenic greenhouse gas (GHG) (Myhre et al., 2013) and the dominant precursor of ozone (O_3)-depleting substances in the stratosphere (Ravishankara et al., 2009). It has an atmospheric lifetime exceeding 100 years (Prather and Wilson, 2026; Prather et al., 2023, 2015; Myhre et al., 2013). Since the preindustrial era, its atmospheric mole fraction has increased from approximately 270 ppb in 1750 to 336 ppb in 2022 (Tian et al., 2024; MacFarling Meure et al., 2006) corresponding to a sustained rise with a mean annual growth rate of $0.96\,\mathrm{ppb\,y^{-1}}$ during the decade from 2010 to 2019 (Tian et al., 2024).

N_2O is emitted to the atmosphere from both natural (65 % of total net emissions) and anthropogenic (35 %) sources (Tian et al., 2024). Among anthropogenic sources, agriculture dominates, accounting for 56% of total net emissions. These emissions primarily arise from the microbial processes of nitrification and denitrification, through which organic and synthetic fertilizers are partially converted to N_2O, as well as from direct nitrogen (N) inputs to soils (Tian et al., 2024; Smith, 2017). Additional significant anthropogenic contributions originate from other direct emissions (32 %), including industry, fossil fuel use, and biomass burning (Tian et al., 2024). The growth rate is expected to increase even further in the future due to the growing demand for food, energy and industrial processes associated with continued population growth (Tian et al., 2024; Smith, 2017; Reay et al., 2012).

This makes N_2O a key target for future mitigation policy (Kanter et al., 2020). To meet the goals of the Paris Agreement (UNFCCC, 2018), limiting global warming to 2 °C requires a reduction in N_2O emissions of 11% by 2050 and as much as 22% to achieve the 1.5 °C limit (Rogelj and Lamboll, 2024; Tian et al., 2024). However, alarmingly, even the worst case Representative Concentration Pathways (RCPs) and Shared Socioeconomic Pathways (SSPs) underestimate the global mean N_2O mole

https://doi.org/10.5194/egusphere-2026-1686
Preprint. Discussion started: 10 April 2026

fractions observed in the atmosphere by roughly 2-3 ppb in 2020 (Tian et al., 2024). Current models sometimes lack adequate representation for N_2O emission factors, for example, for the amount of N soil input or freeze-thaw cycles, which results from a lack of data and measurements for specific regions (Del Grosso et al., 2022; Thompson et al., 2019).

Developing efficient mitigation strategies requires precise quantification of emissions from dominant source sectors and a robust understanding of the underlying processes. N_2O emissions can be estimated using a range of approaches, commonly classified as Bottom Up (BU) and Top Down (TD) methods (Tian et al., 2024; Saboya et al., 2024; CCAC, 2024; Davidson and Kanter, 2014). TD approaches include satellite observations, which offer global coverage but are not yet operational for N_2O (Kiemle et al., 2024). At smaller scales, chamber and tower measurements provide insights at spatial extents of $1\,m^2$ and up to $10\,km^2$, respectively, but are inherently limited to fixed locations (Chadwick et al., 2014; Rapson and Dacres, 2014; Pattey et al., 2007). In contrast, airborne measurements can cover regional scales on the order of 1-100 km and help bridge spatial gaps in the data from chamber and tall tower measurements (Dacic et al., 2024; Pattey et al., 2007). Additionally, in combination with eddy covariance techniques, they further enable improved quantification of emissions from specific sources, which is particularly valuable for the complex and heterogeneous agricultural sector (Waldmann et al., 2026; Smith, 2017).

In the case of N_2O, previously used instruments for high precision N_2O measurements, such as the well established Gas Chromatographs (GCs) or Fourier transform infrared (FTIR) spectrometers with temporal resolutions in the order of 1 min, are being replaced due to the improvement of laser-based measurement techniques and the growing commercial availability of laser spectrometers, allowing for precise (< 1 ppb) and simultaneously faster measurements (~ 1 Hz) (CCAC, 2024; Lebegue et al., 2016; Rapson and Dacres, 2014; Lopez et al., 2012). Particularly, the development of Continuous Wave (CW) Quantum Cascade Lasers (QCLs) working at room temperature opened new possibilities for fast, continuous, more sensitive and more feasible mid-Infrared (IR) absorption spectroscopy (Li et al., 2013; Capasso, 2010) making overly complicated and expensive cooling systems on an aircraft redundant.

Several airborne N_2O in-situ studies using QCLs or other laser-based techniques have already been successfully conducted over the last two decades (Dacic et al., 2024; Eckl et al., 2021; Gvakharia et al., 2020; Kostinek et al., 2019; Gvakharia et al., 2018; Pitt et al., 2016; Xiang et al., 2013; Schiller et al., 2008). However, many of these studies report a temporal resolution of 1 Hz or less, which can be too slow for N_2O eddy covariance measurements on a fast aircraft. Furthermore, airborne measurements still bear more challenges than ground based measurements. During a flight, several parameters may vary considerably, thereby affecting measurement performance. Pitt et al. (2016), Gvakharia et al. (2018) and Kostinek et al. (2019), for example, report dependencies on changes in cabin pressure, roll and pitch angles of the aircraft, and also water vapor (H_2O), which resulted in deviations of some ppb in N_2O. This can be difficult for the precise measurement of small N_2O variability (< 1 ppb) and could be particularly problematic for flights in highly humid regions. Therefore, possible dependencies must be known and addressed by empirical corrections and specific calibration procedures. Furthermore, the space for the instrument setup onboard the aircraft is usually limited, resulting, e.g., in fewer possibilities to carry calibration gases which can impact the calibration procedure and, consequently, data quality.

Here, we present the performance assessment and evaluation of the DLR-MIRO system, a fast (10 Hz sampling frequency) airborne measurement setup specifically tuned for N_2O measurements with an in-flight precision of ~ 0.18 ppb enabling air-

https://doi.org/10.5194/egusphere-2026-1686
Preprint. Discussion started: 10 April 2026

borne eddy covariance measurements for N_2O (Waldmann et al., 2026). The core instrument of the setup is a commercially available Quantum Cascade Laser Absorption Spectrometer (QCLAS), namely a Multicompound Gas Analyzer (MGA^3), from the Swiss company MIRO Analytical AG. We assess the performance of the instrument during in-flight operation onboard two different research aircraft, a Cessna 208-B Grand Caravan operated by the German Aerospace Center (DLR) with an unpressurized cabin and NASA's Douglas DC-8 with a pressurized cabin. The Cessna was deployed on the Greenhouse Gas Monitoring (GHGMon) campaign in the Netherlands in June 2023. The DC-8 was deployed on the NASA Airborne and Satellite Investigation of the Asian Air Quality (ASIA-AQ) campaign in February and March 2024 over the Philippines, South Korea, Taiwan and Thailand. Flights were conducted in humid regions using repeated country-specific flight patterns and vertical profiles. Due to the high variability of H_2O (0-3 %) in tropical environments, we focus on its impact on retrieved N_2O mole fractions. This is particularly important because the original fitting software version v1 did not account for H_2O effects, including both dilution and quantum-mechanical processes such as line broadening. To address this, we derive an empirical water vapor correction based on dedicated laboratory experiments. The results obtained with this correction are compared with those from an updated MIRO fitting software v2, which incorporates a water vapor correction derived from the same experimental dataset from the laboratory. We evaluate and discuss the advantages and limitations of both approaches, including an assessment of the MGA^3 H_2O measurements themselves and the importance for their overall accuracy.

This study is structured as follows: In section 2, we present the specifications of our MGA^3 instrument and the airborne setup, which was identical for both the NASA DC-8 and the DLR Cessna Grand Caravan. We describe the calibration procedure, the basics of the retrieval software v1 of the MGA^3 and elaborate on the relevant parameters for fitting the measured spectra, such as the width of absorption line (β). In Section 3, we first provide an overview of the different water vapor correction approaches applied in this study and describe the laboratory experiment used to derive corresponding parameters for the correction equation. In the next step, we compare the MGA^3 H_2O-measurements to NASA's established Diode Laser Hygrometer (DLH) H_2O-measurements to derive an even more precise water vapor correction. We compare our empirical water vapor correction approaches with a new software version v2 that already implements a water vapor correction based on the same conducted laboratory experiment. We also compare our H_2O-corrected N_2O-measurements with N_2O-measurements conducted by NASA's established Differential Absorption Carbon monOxide Measurements (DACOM) spectrometer (Sachse et al., 1987), a Tunable Diode Laser Absorption Spectrometer (TDLAS) which was also onboard the DC-8 during the ASIA-AQ campaign. In Section 4, we assess the stability of the MGA^3 under ground conditions by calculating its Allan precision and investigate potential dependencies of N_2O-measurements on cabin pressure and roll and pitch angles of the aircraft during flights. In section 5, we present selected flight data from the ASIA-AQ campaign corrected using the different water vapor correction approaches. Finally, we show examples of ambient N_2O measurements from GHGMon and ASIA-AQ to demonstrate the capabilities of the MGA^3 airborne setup under in-flight conditions.

https://doi.org/10.5194/egusphere-2026-1686
Preprint. Discussion started: 10 April 2026

Table 1. Wavenumbers and HITRAN isotopologue numbers of the absorption lines of the target species of laser 1 and laser 2 of the MGA[3].

	wavenumber cm^{-1}	isotopologue number	laser
N_2O	2190.35	446	laser 1
CO	2190.02	26	laser 1
CH_4	1281.61	211	laser 2
H_2O	1281.53	162	laser 2

2 Operational Design

At both the GHGMon and the ASIA-AQ campaign, we operated the same DLR-MIRO setup with a commercially available QCLAS, namely the Multicompound Gas Analyzer (MGA[3]) by the MIRO Analytical AG from Switzerland, as its core instrument. The setup is specifically optimized for N_2O measurements with the capability for the eddy covariance method and up to altitudes of approximately $5.5\,\mathrm{km}$. In the following sections we first describe the specifications of the MGA[3], its integration into the airborne instrument setup, and the data calibration procedure. To provide a better context for our water vapor correction approach, Section 3 outlines the basic theory of spectral fitting and introduces the most important parameters for the water vapor correction as well as the method used by the MGA[3] mole fraction retrieval software.

2.1 Instrument specifications of the MIRO MGA[3]

The MGA[3] is a two-laser (Alpes Lasers; St. Blaise, Switzerland) QCLAS and is able to measure three species at once - N_2O, CH_4, and CO - in addition to H_2O, all within one Herriot measurement cell with a volume of $0.44\,\mathrm{L}$ and an optical path length of $76\,\mathrm{m}$. The wavenumbers scanned by the first laser (laser 1) are $2191.38\,\mathrm{cm^{-1}}$-$2189.85\,\mathrm{cm^{-1}}$ and the wavenumbers of the second laser (laser 2) are $1282.50\,\mathrm{cm^{-1}}$-$1281.01\,\mathrm{cm^{-1}}$ (see Table 1). The MGA[3] is specifically optimized for N_2O measurements by the selection of the spectral absorption lines and the settings defined by the manufacturer. The maximum time resolution of the data retrieval of the instrument is $10\,\mathrm{Hz}$.

The QCLs are driven by an intermittent Continuous Wave (iCW) driving scheme with pulse durations of 10-$100\,\mathrm{s}$ and an overall period of about 0.5-$1\,\mathrm{ms}$. The temperatures of the lasers are held constant at around $32\,^{\circ}\mathrm{C}$ (laser 1) and $-2\,^{\circ}\mathrm{C}$ (laser 2) by ThermoElectric Coolers (TECs). For further general information on the MGAs by MIRO Analytical, please find the paper of Hundt et al. (2018).

2.2 Airborne setup

For the complete functional airborne setup, the MGA[3] requires additional structural components and peripheral devices. First, a liquid chiller (Thermorack401, Solid State Cooling Systems, Wappingers Falls, USA) provides the heat reservoir for the optical compartment of the MGA[3] and the TECs cooling the lasers within the compartment (see section 2.1) as can be seen in Figure 1. The MGA[3] has two inlets, one sample air inlet and one calibration gas inlet. When measuring sample air from outside

https://doi.org/10.5194/egusphere-2026-1686
Preprint. Discussion started: 10 April 2026

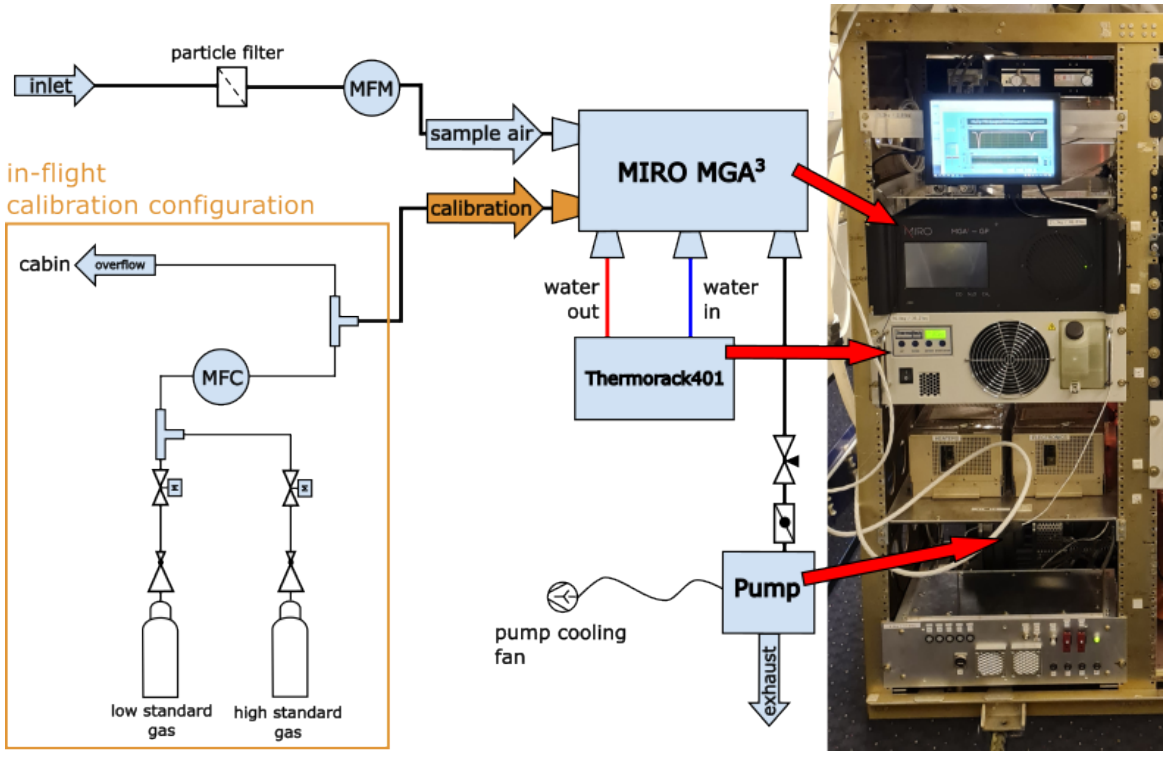

Figure 1. Setup of the instrumentation for both the 2023 GHGmon campaign and the 2024 ASIA-AQ campaign. The left side shows a scheme of the setup including the calibration setup within the orange box. The right side contains a photo of the setup onboard NASA's DC-8 during ASIA-AQ.

the DC-8 aircraft, the air is first drawn through a rear-facing 62 degree trapezoid inlet at the hull of the aircraft and then directed through an about $6.5\,\mathrm{m}$ long PTFE tube with a diameter of $1/2\,\mathrm{in}$ to a $2\,\mu\mathrm{m}$ PTFE-membrane particle filter (filter membrane: R2PJ047 Pall, filter holder: PA1235 Pall). For the Cessna, the PTFE tube was approximately $5.5\,\mathrm{m}$ long and installed through the wing of the aircraft and through its attached wingpod. After filtering the sample air passes a Mass Flow Meter (MFM) (F-102E, Bronkhorst) before it enters the MGA^3 through its sample air inlet. A scroll pump (IS500C, Anest Iwata) connected to the outlet of the MGA^3 is used for creating a vacuum which draws the sample air in. The pump was specifically selected to generate the highest possible mass flow without exceeding the Cessna's power constraints. In this instrument setup with the long inlet tubing, the pump generated a mass flow of $12.5\,\mathrm{slpm}$-$13.8\,\mathrm{slpm}$. The pump motor is additionally cooled with a standard external fan to prevent overheating. Given the MGA^3 cell volume of $0.44\,\mathrm{L}$ and a cell pressure of $70\,\mathrm{hPa}$ this corresponds to an effective sampling frequency of 6.85-$7.57\,\mathrm{Hz}$, assuming plug flow. To achieve higher mass flows, and therefore higher effective sampling frequencies, we recommend minimizing the distance between the aircraft inlet and the instrument.

https://doi.org/10.5194/egusphere-2026-1686
Preprint. Discussion started: 10 April 2026

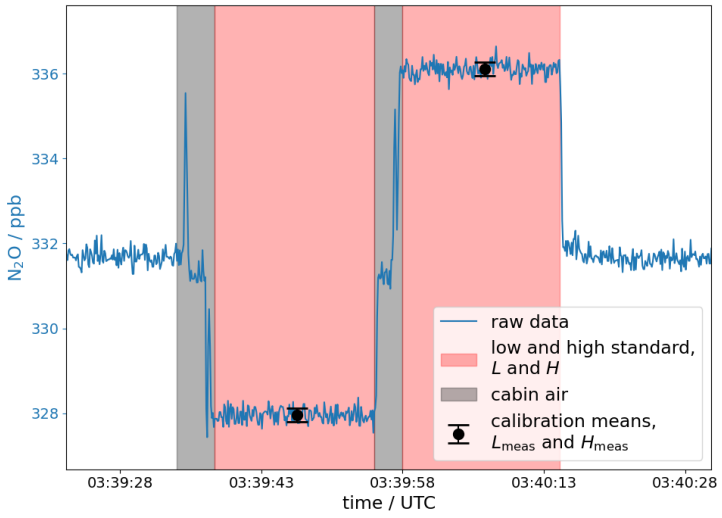

Figure 2. Example of an in-flight two-point calibration from the ASIA-AQ campaign. When a calibration sequence is activated first an internal valve of the MGA^3 switches from the sample air inlet to the calibration gas inlet. Then, during the first time span (gray area), cabin air is drawn in via the overflow of the calibration system. Shortly after the solenoid valve for the low standard calibration gas L is activated for about 20 s allowing the gas to be drawn in by the MGA^3 (first red area). Then the solenoid valve closes and cabin air is shortly drawn again (second gray area) until the second solenoid valve activates for the high standard calibration gas H (second red area). In total the calibration process lasts for about 40 s. The black dots are the mean values L_{meas} and H_{meas} of L and H with their respective errors, which are then used for the calibration to relate to the known reference values of the calibration gases.

2.3 Calibration of data and response time

In this section, we describe the calibration procedure applied to our data to account for drifts and potential changes in the sensitivity of the MGA^3 and determine the response time of the system. To avoid drift and sensitivity effects of GHG measurements and to improve the accuracy of the retrieved mole fractions, the instrument needs to be regularly calibrated in-flight using a two-point calibration. For this, the MGA^3 switches an internal valve and then draws air not from the sample air inlet but from the calibration gas inlet which is connected to an in-flight calibration system (see Figure 1, orange box). As can be seen from the measurements in Figure 2, as an example from ASIA-AQ, every 10 min two calibration gases are drawn, a low-standard calibration gas L and a high-standard calibration gas H, each for 20 s in sequence. Two solenoid valves are operated directly from the MGA^3 software and they control which of the two gases is currently being used. The red areas show the L and H standards, and the grey areas show when cabin air is sampled through the overflow while switching the main MGA^3 valve from the sample air inlet to the calibration gas inlet. When the main valve of the MGA^3 switches to cabin air in the first gray area or when the solenoid valves switch to the calibration gases, the initial high pressure coming from the cabin or the cylinders results in a feedback behavior leading to a time of 1-2 s for the cell to be completely flooded by the cabin air or the calibration gases. When switching the valves back to the cabin air in the second grey area in Figure 2 or back to ambient sampling air after the

https://doi.org/10.5194/egusphere-2026-1686
Preprint. Discussion started: 10 April 2026

Table 2. Mole fraction values of each high and low standard gas pair for the GHGMon and ASIA-AQ campaign.

	N_2O low standard / ppb	N_2O high standard / ppb
GHGMon 1	344.85	347.35
GHGMon 2	344.63	346.65
ASIA-AQ 1	333.99	342.23
ASIA-AQ 2	330.47	340.65
ASIA-AQ 3	331.32	339.03

second red area, this effect does not occur. With these two cases we determine our response time of 0.1-$0.2\,\mathrm{s}$ which confirms our effective sampling frequency of approximately $7\,\mathrm{Hz}$ determined with the mass flow through the cell in Section 2.2. More details on the calibration times will be shown in Section 4.1. The Mass Flow Controller (MFC) (F-201CV, Bronkhorst) behind the solenoid valves is set to a higher flow than the instrument consumes ($15\,\mathrm{slpm}$) and any excess flow of the calibration gases in front of the MGA[3] inlet is released to the cabin via an overflow. All in-flight calibration gas standards for N_2O are chosen to be close to the atmospheric background mole fractions and were themselves calibrated on the ground against NOAA-standards (traceable to the NOAA-N2O_X2006A reference scale). In Table 2, the N_2O mole fractions of the two different high and low standards used during the GHGMon campaign and the three different high and low standards used during the ASIA-AQ campaign are shown. High and low standards were chosen to have a difference of 10-$20\,\mathrm{ppb}$ to be able to cover the small variability in N_2O caused by agricultural emissions.

To calculate the calibrated time series $X_{\mathrm{cal}}(t)$ out of a measured raw data time series $X_{\mathrm{raw}}(t)$ that is provided by the MGA[3], we first calculate a scale factor m_n and an offset d_n for each calibration cycle $n = 1, \ldots, N$ for all $N \in \mathbb{N}$ cycles, according to Pitt et al. (2016) with:

$$m_n = \frac{H_{\mathrm{true}} - L_{\mathrm{true}}}{H_{\mathrm{meas,n}} - L_{\mathrm{meas,n}}}, \qquad n = 1, \ldots, N;\, N \in \mathbb{N} \tag{1}$$

$$d_n = H_{\mathrm{true}} - m_n \cdot H_{\mathrm{meas}}\,. \tag{2}$$

Here $H_{\mathrm{meas,n}}$ and $L_{\mathrm{meas,n}}$ are the means of the measured values for the high and low standards H and L as shown for one calibration cycle n in Figure 2. H_{true} and L_{true} represent their known true mole fractions in Table 2. We interpolate the scale factors m_n and offsets d_n between every calibration cycle for every time point t in the measured time series $X_{\mathrm{raw}}(t)$ and get the continuous scale factor $m(t)$ and offset $d(t)$ which lead us to the calibrated values $X_{\mathrm{cal}}(t)$:

$$X_{\mathrm{cal}}(t) = m(t) \cdot X_{\mathrm{raw}}(t) + d(t)\,. \tag{3}$$

For our H_2O measurements, we only use a one-point-calibration, since both L and H standards are dry and should not contain any H_2O. Here, we calculate the difference d_n between the mean $V_{\mathrm{meas},n}$ of a measured calibration cycle of only one of the

https://doi.org/10.5194/egusphere-2026-1686
Preprint. Discussion started: 10 April 2026

two cylinders and its known actual value V_{true}. We obtain the calibrated value $X_{\mathrm{cal}}(t)$ by interpolating d_n for every t to $d(t)$:

$$d_n = V_{\mathrm{true}} - V_{\mathrm{meas},n} \qquad n = 1,\ldots,N;\, N \in \mathbb{N} \tag{4}$$

$$X_{\mathrm{cal}}(t) = X_{\mathrm{raw}}(t) + d(t)\,. \tag{5}$$

For the uncertainty of our cylinders we use the standard error for every mean calculated from the L and H standards in the calibration cycles resulting in uncertainties below $1\,\mathrm{ppb}$. Experience from GHGMon showed that the respective differences between the standards of about $3\,\mathrm{ppb}$ in N_2O were too small causing issues while calibrating the data, especially with the error calculation for the calibration procedure. Based on this and the later experience from ASIA-AQ flights, we recommend that the differences between the high and low standards including the errors of the cylinder values should be at least two orders of magnitude higher than the precision of the MGA^3.

2.4 MGA^3 mole fraction retrieval software and versions

In this section, we explain how the MGA^3 software retrieves the mole fraction values C from its measurements. The lasers of the MGA^3 emit light in a wavenumber range close to the absorption lines of the target species such as N_2O. The laser beam is directed into the measurement cell where the target sample air is located. There, the intensity I_0 of the laser beam weakens through absorption by the sample air. After the laser beam exits the cell, it illuminates a detector which measures the intensity I along the wavelengths, i.e. the absorption spectrum and therefore the absorption line profile of the N_2O. Each measured spectrum is then provided as the transmittance $\tau(\nu)$ by the MGA^3. The measured absorption line profile can either be fitted online while measuring or later on at any time with the MGA-ReFit software. The lines are fitted by minimizing the sum of least-squares using the Beer-Lambert law, which in this case is based on a Voigt profile:

$$\tau(\nu) = \frac{I(\nu)}{I_0(\nu)} = \exp(-\alpha(\nu,p,T)\cdot N_0(p,T)\cdot L\cdot C)\,. \tag{6}$$

Here N_0 is the Loschmidt constant and ν represents the wavenumber. By knowing the pressure p, the temperature T and the optical path length L of the measurement cell, the software can calculate the absorption coefficient α and the mole fraction C of the measured species (Hundt et al., 2018). The absorption coefficient α represents the shape of the Voigt profile for a specific molecule including the Half-Width-Half-Maximum (HWHM) of its absorption line profile if only one such molecule is observed (see Appendix A). The mole fraction C then scales α for more than one molecule.

In this paper we use two different versions of the MGA^3 fitting software. The original software of our MGA^3 model, which we denote as version 1 (v1) (V30.0.171.0), does not correct for water vapor dependencies. That means that it fits each measured absorption line applying Equation 6 and calculates the mole fraction C, but does not account for dilution and it cannot account sufficiently enough for all quantum-mechanical effects, such as water vapor line broadening, on the data, since not all processes are known or can be determined. To correct for these water vapor dependencies we conducted a water vapor experiment in the laboratory which we use to determine an empirical water vapor correction as shown in Section 3. This correction is then applied during the data post-processing to the already retrieved C time series. In parallel, an updated version of the fitting software was developed by MIRO Analytical. The new version is based on the same laboratory experiment and now includes a correction

https://doi.org/10.5194/egusphere-2026-1686
Preprint. Discussion started: 10 April 2026

for water vapor dilution and broadening effects already implemented in the fitting process of the spectra. The software version (V30.1.59.0) is in the following referred to as version 2 (v2). The resulting v2 time series of the retrieved mole fractions C does not longer require the postfit corrections as in v1.

2.5 Fitting with constant HWHM - the β option

For the software version v1, the MGA[3] has the option to activate or deactivate the β, which is, within the MIRO software, an internal measure for the HWHM of each absorption line and therefore for the absorption coefficient α (see Appendix A). If the β is deactivated, the MGA[3] freezes the HWHM of the respective absorption line for all upcoming spectra and uses the last used value when the β was still active. This means, however, that consequently the mole fraction C in the fitting function 6 has to account for any changes that would occur in α. This leads to deviations from the actual values in C. However, with high water vapor contents in the sample air, as we show in Appendix A, the HWHM solely depends on water vapor for our N_2O spectral line. Based on this, the mole fraction C time series with a frozen β can subsequently be corrected by an empirical water vapor correction. In the following, we denote this water vapor corrected data as v1-β-off. To enforce the same behavior for all v1-β-off refit-processes as much as possible, we deactivate the β always when dry gas is measured and therefore no water vapor should be present.

At this point, the mole fractions retrieved by v1-β-off should not differ compared to water vapor corrected data retrieved with v1 and an activated β - from here on denoted as v1-β-on. However, due to the α being kept constant in v1-β-off the fitting software has one parameter less to account for in the fitting process which results in less numerical noise in C compared to v1-β-on. Software version v2 does not have a β option an already corrects for water, and therefore will be simply denoted as v2. These correction approaches will now be discussed in more detail in the next Section 3.

3 Water vapor correction approaches of N_2O in this study

Water vapor is highly variable in the atmosphere with $1\text{-}10\,\mathrm{ppm}$ in the Upper Troposphere - Lower Stratosphere (UTLS) (Kaufmann et al., 2016) and even up to $30000\,\mathrm{ppm}$ within the tropical boundary layer as shown in Figure 5 from the ASIA-AQ measurements. Due to this high variability of water vapor in different regions of the world and its volatility, GHG measurements are usually reported in dry mole fractions for better comparability, which requires precise water vapor measurements at all times. The first step is to eliminate the dilution from the gas due to the present H_2O by using the following equation:

$$C_{\mathrm{dry}} = \frac{C_{\mathrm{wet}}}{1 - C_{\mathrm{H_2O}}}. \tag{7}$$

Here, C_{wet} denotes the mole fraction of N_2O diluted by H_2O. $C_{\mathrm{H_2O}}$ is the mole fraction of the H_2O and C_{dry} represents the mole fraction of N_2O in the gas mixture after the removal of H_2O. However, additional spectroscopic effects, such as water vapor line broadening, or instrument-specific behaviors in the measurements can have an impact on the data if not accounted for correctly or not at all. Those effects then often have to be corrected by using an empirical water vapor correction, also specific to each instrument (e.g. Pitt et al. (2016) and Gvakharia et al. (2018)).

https://doi.org/10.5194/egusphere-2026-1686
Preprint. Discussion started: 10 April 2026

Since the original MGA^3 software v1 does not provide a water vapor correction, neither for dilution nor completely for spectroscopic effects, we first derive an empirical water vapor correction from a laboratory experiment, further described in Section 3.1. With the parameters a_0 and b_0 determined from a quadratic function in the laboratory, we apply the following water vapor correction equation also used by Rella et al. (2013) to account for all potential H_2O dependencies:

$$C_{\mathrm{dry}} = \frac{C_{\mathrm{wet}}}{a_0 \cdot C_{\mathrm{H_2O}}^2 + b_0 \cdot C_{\mathrm{H_2O}} + 1}, \tag{8}$$

which we will explain more thoroughly in Section 3.2. In the following, we shortly introduce how we attain four water vapor corrected mole fraction data sets, retrieved from a single measured spectral data set, by different approaches.

v1-β-on

The wet mole fractions C_{wet} for N_2O and $C_{\mathrm{H_2O}}$ for H_2O are retrieved by the software version v1 and with an activated β. The time series C_{wet} is then water vapor corrected to obtain C_{dry} by using Equation (8). The data for the lab experiment from which we derive our correction is also fitted with the software version v1 with an active-β (see Section 3.1).

v1-β-off

This approach is identical to v1-β-on except that the β is deactivated during all fitting and retrieval processes by the MGA^3 software.

v1-β-off-DLH

A precise water vapor correction approach requires precise water vapor measurements. Hence, for this specific approach, we first retrieve the wet mole fractions C_{wet} for N_2O and $C_{\mathrm{H_2O}}$ for H_2O with a deactivated β, as for v1-β-off, and then compare our MGA^3-H_2O measurements to the H_2O measurements made by NASA's well established Diode-Laser-Hygrometer (DLH) at the ASIA-AQ campaign (Diskin et al., 2002). Thereby, we checked the stability of the MGA^3 water vapor measurements over multiple flights and adjusted the MGA^3-H_2O measurements accordingly to the DLH-H_2O measurements to achieve the same standard for the MGA^3-H_2O measurements over all the flights (see Section 3.3 for more details). The mean behavior of the MGA^3-H_2O measurements of all flights compared to the DLH-H_2O measurements is also used to calibrate the the MGA^3-H_2O measurements from the laboratory experiment from which the water vapor correction is derived. Then the DLH-adjusted $C_{\mathrm{H_2O}}$ and the DLH-adjusted correction function from the laboratory experiment are used for correcting C_{wet} to C_{dry} using the correction function (8).

v2

In this approach, we use the newly implemented MGA^3 retrieval software v2 which already includes a water vapor correction based on the same laboratory experiment as used for the previous approaches. The water vapor correction, however, is applied already while fitting the spectra and not after the N_2O mole fraction C_{wet} is retrieved. Here, the H_2O spectra are directly used to

https://doi.org/10.5194/egusphere-2026-1686
Preprint. Discussion started: 10 April 2026

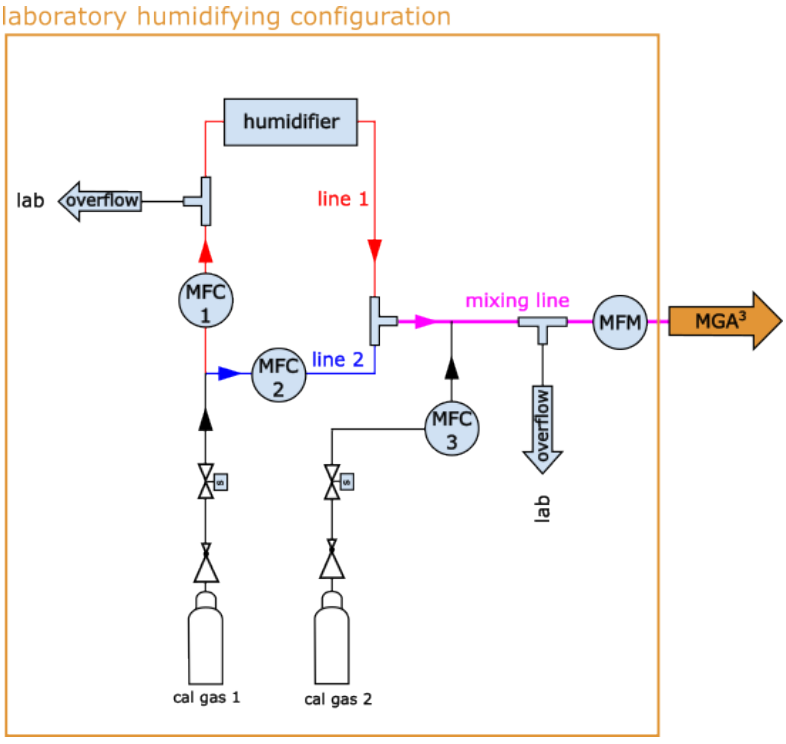

Figure 3. Scheme of the setup of the water vapor laboratory experiment. To fully function the orange box gets exchanged with the orange box of the in-flight calibration configuration in Figure 1.

correct the N_2O spectra and directly report corrected C_{dry} mole fractions. The H_2O spectra or measurements are not adjusted to the DLH measurements beforehand as for v1-β-off-DLH.

3.1 Laboratory Experiment

In this chapter, we explain the setup of the laboratory experiment for the water vapor correction, how we conducted it and how we prepared the data retrieved from this experiment for the water vapor correction equation. For the laboratory experiment, we change the calibration system in Figure 1 from the "in-flight calibration" configuration to the "laboratory humidifying" configuration in Figure 3 and only use the calibration gas inlet of the MGA^3 throughout the whole experiment. The sample gas is provided by a gas cylinder (cal gas 1) and is first divided into two sub-lines, which are controlled by a mass flow controller each. One sub-line (line 1) is provided only $3\,\mathrm{slpm}$ by its mass flow controller (MFC 1), since the humidifier (Dew Point Generator LI-610, LICOR) only operates with mass flows up to $2.5\,\mathrm{slpm}$. The excess gas in line 1 is then released through the overflow behind the MFC 1 to protect the humidifier. The output of the humidifier is controlled in a range of $0\,\mathrm{slpm}$-$2.5\,\mathrm{slpm}$ with a valve on the humidifier itself. The second sub-line (line 2) is provided with $0\,\mathrm{slpm}$-$5\,\mathrm{slpm}$ by the MFC 2 which directly merges with the humidified output from line 1. The length of the mixing line is $1.5\,\mathrm{m}$ to allow for optimal mixing of dry gas

https://doi.org/10.5194/egusphere-2026-1686
Preprint. Discussion started: 10 April 2026

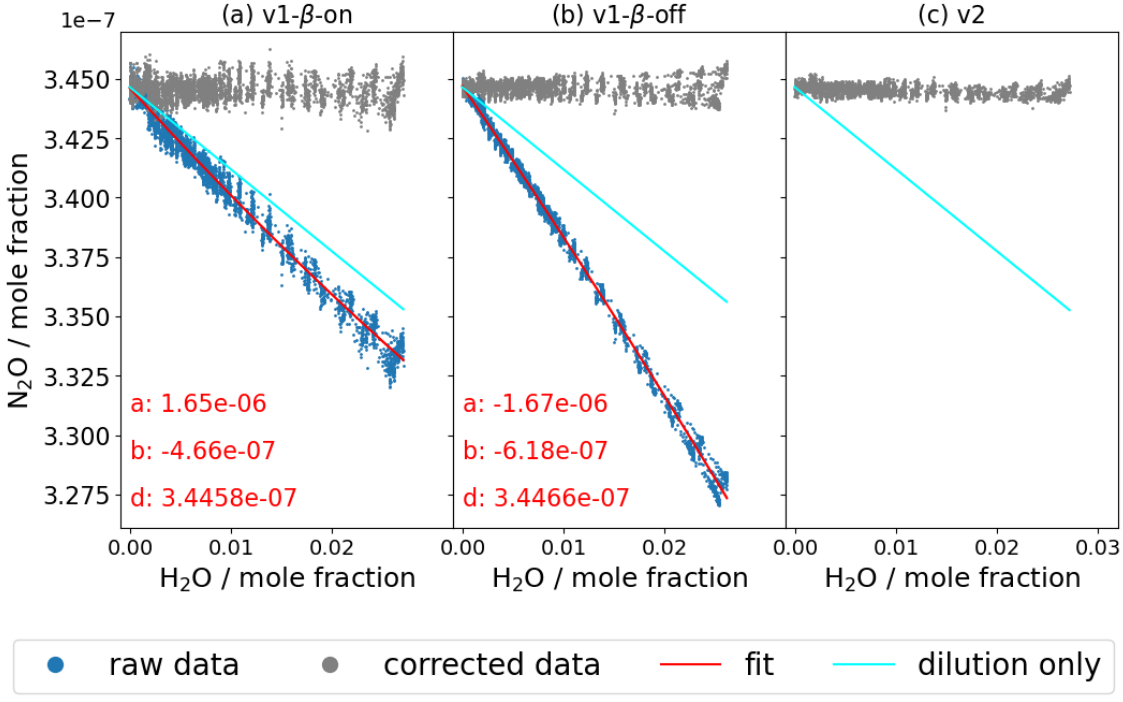

Figure 4. In (a) and (b) we can see the behavior of the raw N_2O with increasing H_2O mole fractions (blue dots) during laboratory water vapor experiment for v1-β-on and v1-β-on. The red lines are fitting functions giving us the parameters for our water vapor correction function in section 3.2. The cyan line shows the expected behavior of the raw mole fractions if only dilution was having an effect on the measurements. The grey dots are the blue dots corrected by the water vapor correction function (17) in section 3.2. In (c) the grey dots represent the raw mole fraction output of the experiment when reprocessed with version v2 of the MGA-ReFit software. The data were are already corrected for water vapor influences based on the same data in (a) and (b) while they were being reprocessed.

and humidified gas. The merged gas then directly flowes into the MGA[3], which is set to operate with a mass flow of $1.9\,\mathrm{slpm}$ for this experiment. The excess gas in the mixing line is released through an overflow in front of the MGA[3]. The second gas, cal gas 2, is used only for calibration purposes. The settings are the same as in the airborne setup at the GHGMon and the ASIA-AQ campaigns (see Section 2.2) with a cell pressure of $70\,\mathrm{hPa}$ and a cell temperature T of $25\,^{\circ}\mathrm{C}$.

For the experiment, the MFC 2 is first set to $5\,\mathrm{slpm}$ and the humidifier output to $0\,\mathrm{slpm}$, allowing only for the dry gas from cylinder 1 to be sampled. Then, the output of the humidifier is increased stepwise from $0\,\mathrm{slpm}$ to $2.5\,\mathrm{slpm}$, increasing the mole fraction of water vapor in the mixing line. Once the maximum mass flow for the humidifier output is reached, the mass flow of MFC 2 is incrementally decreased from $5\,\mathrm{slpm}$ to $0\,\mathrm{slpm}$, further increasing the humidity in the merged gas until only the output from the humidifier is sampled. Thereby, a range of water vapor mole fractions of 0-3 % is covered. This process of humidifying is repeated four times. Before and after each repetition, the gas from cylinder 2 is sampled for calibration purposes.

https://doi.org/10.5194/egusphere-2026-1686
Preprint. Discussion started: 10 April 2026

The recorded spectral data are then refitted with three different water correction approaches. Twice with the original software version v1 (once with an activated β and once with a deactivated β) and once with the updated version v2. Figure 4 shows the retrieved N_2O mole fractions from all those three approaches versus the retrieved H_2O mole fractions after calibrating the time series to the dry cylinder gases. As obvious from Figure 3 (a) and (b) for v1, the uncorrected N_2O (blue dots) mole fraction varies by more than $10\text{-}18\,\mathrm{ppb}$ in humid versus dry conditions. The cyan line gives the expected impact of the dilution effect only compared to dry conditions. In (a) and (b) the measured raw data deviate from the expected behavior due to spectroscopic effects, which not all can be accounted for by the software in general. Furthermore, we only use an one-point calibration for the H_2O measurement, which could be a reason for the deviations from the cyan line. Since we use dry calibration gas in both cylinders, we cannot account for changes in sensitivity of the H_2O measurements for values above 0. With the deactivated, frozen β in v1 the deviation is larger than with the activated β-on since the water vapor line broadening is not accounted for in this setting (see Section 2.5). Figure 4(c) shows the mole fractions retrieved with the updated software version v2, in which the N_2O mole fractions are already corrected for water vapor during the fitting process of the measured spectra (grey dots). For the raw data in Figure 4(a) and (b) we first have to derive a correction which leads us to the corrected data sets v1-β-on and v1-β-off (grey dots). This, we show in the next Section 3.2.

3.2 Water Correction Function

In the next step, we correct the raw N_2O data in Figure 4(a) and (b) and derive a water vapor correction function. For this, the wet raw data $C_{\mathrm{lab,wet}}$ given in Figure 4(a) and (b) are fitted with a quadratic function (red line), giving us the parameters a, b, d:

$$\mathrm{fit}(C_{\mathrm{H_2O}}) = a \cdot C_{\mathrm{H_2O}}^2 + b \cdot C_{\mathrm{H_2O}} + d\,. \tag{9}$$

Here, $C_{\mathrm{H_2O}}$ is the H_2O mole fraction. In an ideal fit, the parameter d represents the actual value of the dry cylinder mole fraction for $C_{\mathrm{H_2O}} = 0$ and therefore simultaneously the dry target value after the water vapor correction is applied for all $C_{\mathrm{H_2O}}$. To obtain the water vapor corrected mole fraction $C_{\mathrm{lab,dry}} = d$ for N_2O in this laboratory experiment, the value of the correction function 9 is subtracted without the parameter d from $C_{\mathrm{lab,wet}}$:

$$C_{\mathrm{lab,dry}} = C_{\mathrm{lab,wet}} - (a \cdot C_{\mathrm{H_2O}}^2 + b \cdot C_{\mathrm{H_2O}})\,. \tag{10}$$

However, the parameters of this fit function apply only for the specific mole fraction d of the used cylinder and not necessarily for cylinders with random mole fractions C_{dry}. If a humidified air sample containing no N_2O were sampled, these specifically determined parameters would still produce a correction value for the corresponding $C_{\mathrm{H_2O}}$, despite the absence of the N_2O. To account for any other values C_{dry} in the cylinder, we use following boundary condition:

$$C_{\mathrm{dry}} = 0 \Leftrightarrow \mathrm{fit}_x(C_{\mathrm{H_2O}}) = 0 \qquad \forall C_{\mathrm{H_2O}} > 0 \tag{11}$$

$$\Rightarrow a, b, d = 0 \tag{12}$$

https://doi.org/10.5194/egusphere-2026-1686
Preprint. Discussion started: 10 April 2026

and assume that the parameters a, b and c - consequently the fit Equation 9 - approach 0 proportionally with decreasing mole fractions C_{dry}, giving:

$$a = \frac{a-0}{d-0} \cdot C_{\mathrm{dry}} = \frac{a}{d} \cdot C_{\mathrm{dry}} = a_0 \cdot C_{\mathrm{dry}}\,, \tag{13}$$

$$b = \frac{b}{d} \cdot C_{\mathrm{dry}} = b_0 \cdot C_{\mathrm{dry}}\,, \tag{14}$$

$$d = \frac{d}{d} \cdot C_{\mathrm{dry}} = d_0 \cdot C_{\mathrm{dry}} = C_{\mathrm{dry}}\,, \tag{15}$$

$$C_{\mathrm{dry}} = C_{\mathrm{wet}} - (a_0 \cdot C_{\mathrm{dry}} \cdot C_{\mathrm{H_2O}}^2 + b_0 \cdot C_{\mathrm{dry}} \cdot C_{\mathrm{H_2O}})\,. \tag{16}$$

C_{wet} is the measured wet mole fraction of N_2O using the new cylinder with C_{dry}. The fit parameters in (13)-(15) are now dependent on the mole fractions C_{dry} in the cylinder and from equation (16) we get:

$$C_{\mathrm{dry}} = \frac{C_{\mathrm{wet}}}{a_0 \cdot C_{\mathrm{H_2O}}^2 + b_0 \cdot C_{\mathrm{H_2O}} + 1}\,, \tag{17}$$

which can finally be used for any random measurement C_{wet} with a simultaneously measured $C_{\mathrm{H_2O}}$. Equation 17 is the same as the one used by Rella et al. (2013), also with the assumption that the water vapor correction is proportional to the mole fraction of our observed species.

The correction Equation (17) is then applied to the raw data in Figure 4(a) and (b) and results in the grey corrected data v1-β-on and v1-β-off. With this, our retrieved data is corrected for water vapor and influences and should be independent of water vapor changes either by dilution or spectral effects like line broadening. The main difference between the β-on and β-off retrieved data is that the noise in the data for the β-off data is smaller (see Section 2.5) by roughly 70 % compared to its respective β-on retrieved data, which will be discussed in Section 3.5 in more detail.

3.3 H_2O calibration against DLH absolute ambient measurements

The quality of the water vapor measurement is decisive for a precise water vapor correction. While the absolute accuracy is not of main importance, the stability of the water vapor measurement is, hence, the replicability of the H_2O measurements over time. To analyze the stability of the MGA^3-H_2O measurements in our setup, we compare data from 14 flights from the ASIA-AQ campaign with absolute ambient H_2O vapor measurements measured by the established DLH. We use the DLH because it reliably reports stable water vapor measurements which can be used to effectively correct the MGA^3 water vapor measurements. In our airborne measurement setup the MGA^3 is only calibrated by an one-point calibration using our dry cylinder gases (see Section 3.1), leading to differences in the data between the two instruments. In Figure 5(a) the DLH-H_2O for each of the 14 flights is plotted against the respective MGA^3-H_2O data for the β-off setting. The flights were conducted over a time span of roughly two months. The lines are polynomial fits (second order) of the measurements, calculated by applying orthogonal distance regressions. The dashed red line shows a slope of 1. The dashed black line shows the mean of all curves, which is also a quadratic function described with $f(x) = ax^2 + bx + d$. The difference in the length of every curve is due to the differences in the maximum measured humidity during each flight.

https://doi.org/10.5194/egusphere-2026-1686
Preprint. Discussion started: 10 April 2026

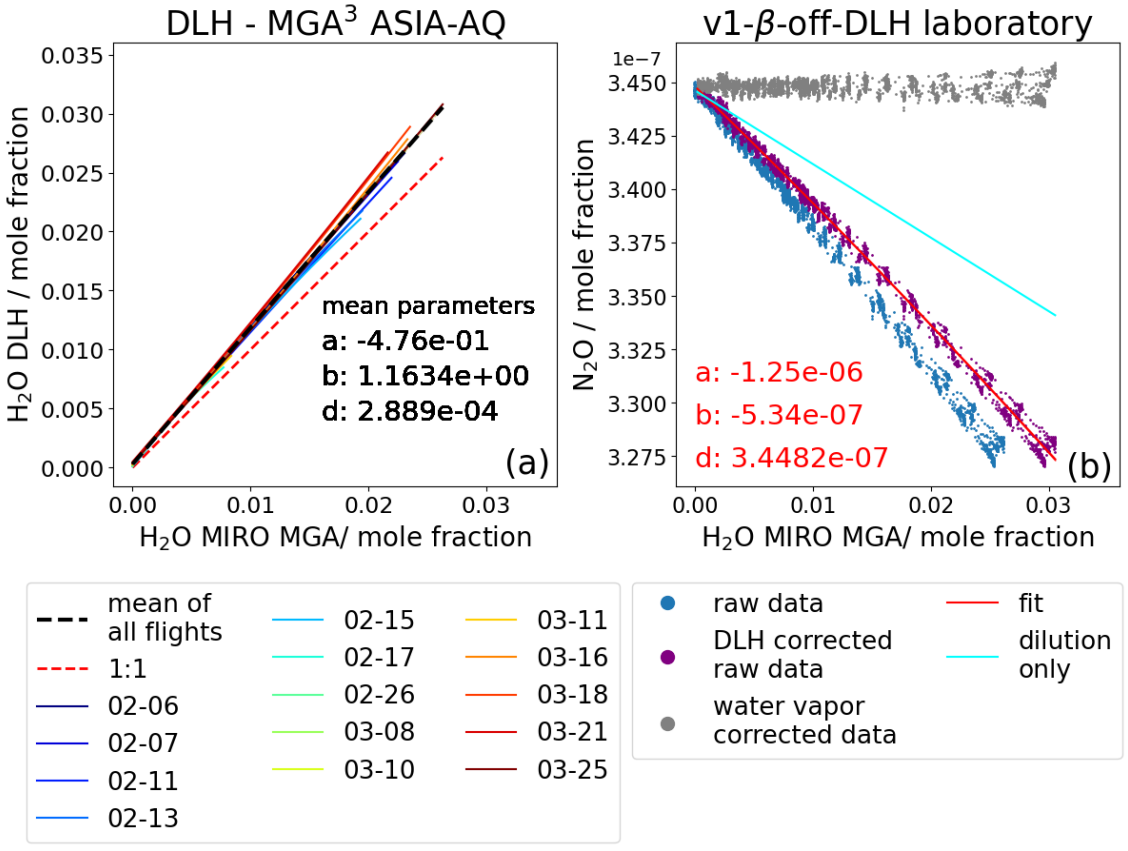

Figure 5. In (a) we plotted the DLH-H_2O measurements against the MGA^3-H_2O measurements for the mole fractions retrieved with v1 with a deactivated β for 14 ASIA-AQ flights from February 6th to March 25th. In general, our instrumental setup measured less H_2O than DLH. With increasing H_2O the MGA_3 measurements seem to deviate more from each other indicating changes in sensitivity of the instrument. The black dashed lines show the mean for all flights. Figure 5(b) shows again the same as Figure 4 (b) but now the blue raw data is first corrected by the respective dashed black line in Figure 5(b) resulting in the "DLH-corrected" purple dots. The red lines are now the fitting lines for the purple data, which parameters now can be used to derive the new correction v1-β-off-DLH.

In general, the DLH measures about $b = 1.16$ times higher H_2O values than the MGA3 with our instrumental setup, which is mainly due to not being able to conduct a two-point-calibration as mentioned. Other minor reasons could be, for example, water vapor tube dampening effects through the long $6.5\,\mathrm{m}$ PTFE inlet tubing in our setup. At the instrument flow rate of approx. 13 slpm, it takes about $2\,\mathrm{s}$ at $1\,\mathrm{atm}$ until the sample air reaches the measuring cell, during which water vapor could attach and slowly unstick from the inner tubing walls. Still, the results show that the correlation of both H_2O measurements for the flights diverge for higher H_2O values, indicating changes in the sensitivity. In principle, this can only be accounted for by a sufficient two-point-calibration as explained in Section 3.2. The changing behavior over the flights, however, means that

https://doi.org/10.5194/egusphere-2026-1686
Preprint. Discussion started: 10 April 2026

Table 3. Percentage of how many data points of the DACOM measurements overlap with MGA^3 data with different water vapor correction approaches applied within the combined uncertainties at 5 Hz.

flight	v1-β-off / %	v1-β-off-DLH / %	v2 / %
2024-03-25	74.5	74.4	60.8
2024-03-21	53.1	79.4	55.9
2024-03-18	70.1	82.3	62.1

the once attained correction equation in the laboratory will behave slightly differently for every flight unless the MGA^3-H_2O is not standardized to a norm.

To account for this variability in behavior of the MGA^3-H_2O from flight to flight, we constructed a new correction specifically for all the ASIA-AQ flights in addition to the already existing v1-β-off approach in chapter 3.2, called v1-β-off-DLH, which can be seen in 5 (b) (grey dots). First, since the H_2O measurement in the laboratory water vapor experiment cannot be calibrated against absolute reference values - due to our used humidifying configuration setup not being able to provide such an accurate value - we assume that the H_2O behavior in the experiment is similar to the mean behavior of all flights (dashed black line in Figure 5(a)). Thus, we correct our laboratory experiment H_2O values with this mean (see Section 3.4 for explanation). This results in the purple DLH corrected data in Figure 5(b). We can see that the DLH adjusted N_2O raw data is closer to the cyan line which represents the ideal behavior if only dilution existed. Now, the fit (red line) is used for deriving the parameters of our water vapor correction in the same way as for v1-β-off. However, before the correction function is applied to the flight data, we first correct the H_2O flight measurements with their respective line in Figure 5(a) to assure, that all flight measurements and the laboratory H_2O measurements are "calibrated" to the same standard, which in this case are the DLH measurements. Now, the water vapor correction function can be applied to the flight data giving the water vapor corrected mole fraction data. This approach is denoted as v1-β-off-DLH.

In the next section, we compare the results from the different correction approaches v1-β-off, v1-β-off-DLH and v2.

3.4 Comparison of the different water correction approaches

In this chapter, we compare the data retrieved by the different MGA^3 software versions and water correction approaches v1-β-off, v1-β-off-DLH and v2 with the data measured by NASA's established DACOM spectrometer. The DACOM is a TDLAS designed for CO measurements but it also measures CH_4 and N_2O. It has a temporal resolution of 5 Hz and dries the sample air via a Nafion tube before sampling, negating water vapor interference and dilution effects. Our calibration cylinders for the MGA^3 were cross calibrated against the NOAA calibration cylinders of DACOM. This makes the DACOM measurements ideal for the validation of our water vapor correction approaches for the MGA^3-N_2O measurements. For a better comparison, the MGA^3 data was resampled to 5 Hz to match the DACOM data. We chose to compare three flights in Thailand for which data from both instruments are available, well calibrated and, most importantly, high H_2O variability was measured.

https://doi.org/10.5194/egusphere-2026-1686
Preprint. Discussion started: 10 April 2026

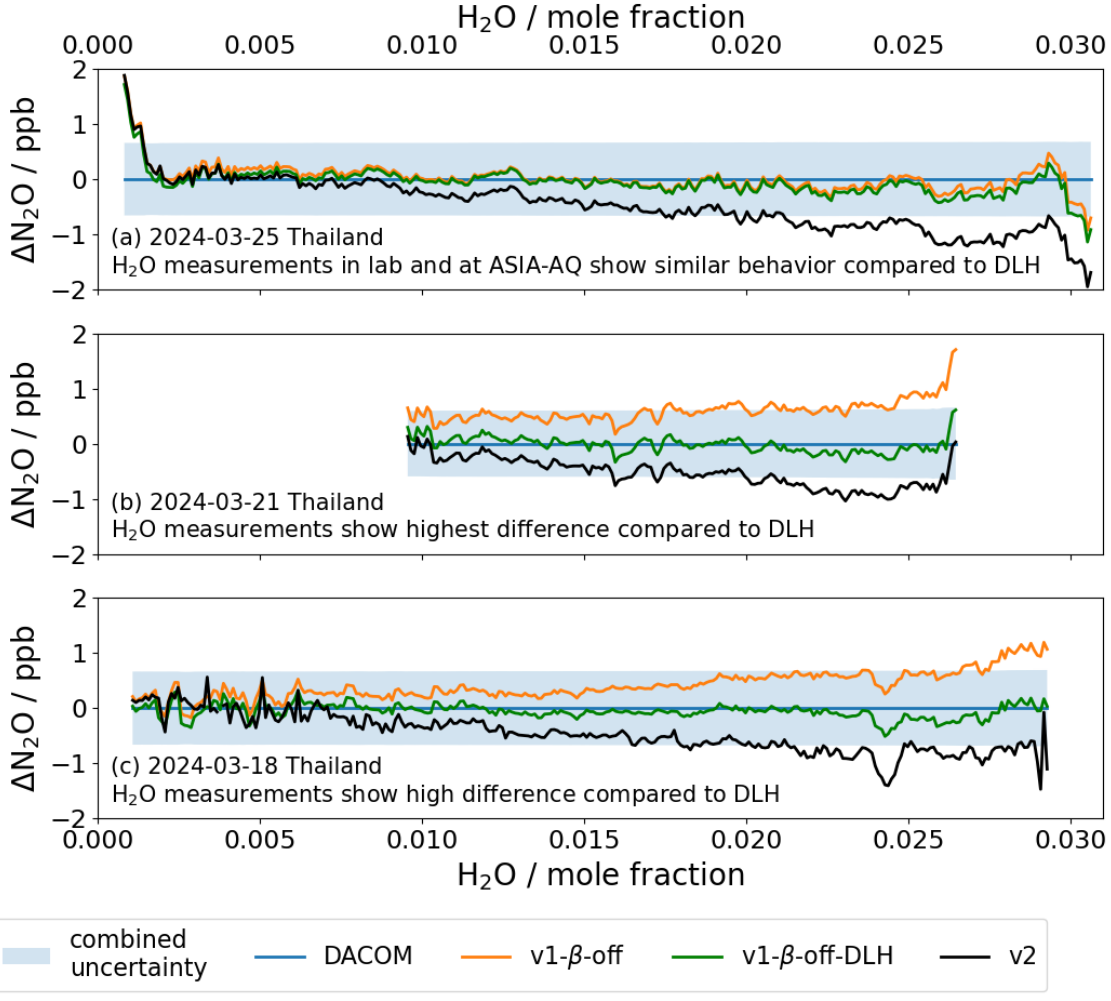

Figure 6. Differences between N_2O data measured by DACOM and the MGA[3] for the different water vapor correction approaches v1-β-off, v1-β-off-DLH and v2 for three ASIA-AQ flights on the 2024-03-25 (a), 2024-03-21 (b) and 2024-03-18 (c). The colored lines show the mean values of the differences between DACOM and the MGA[3] corrected data in $0.01\,\%$ or $100\,\mathrm{ppm}$ H_2O bins. The shaded blue areas represent the combined uncertainties of DACOM and the MGA[3] with v1-β-off-DLH but at full resolution and not with the $0.01\,\%$ bin resolution.

Figure 6(a), (b) and (c) illustrates the difference between the DACOM-N_2O data and the MGA[3]-N_2O for three selected ASIA-AQ flights (2024-03-25, 2024-03-21 and 2024-03-18). Different colors represent data retrieved using the different MGA[3] approaches (v1-β-off in orange, v1-β-off-DLH in green and v2 in black). The lines represent the mean values for $0.01\,\%$ ($100\,\mathrm{ppm}$) H_2O bins. The blue shaded areas show the combined uncertainties of the DACOM measurements and the v1-β-off-DLH data. However, for the combined uncertainties, we do not use the $0.01\,\%$ H_2O bins resolution, but uncertainties of the full $5\,\mathrm{Hz}$ resolution to capture the variability of the instruments more accurately. Since our MGA[3] calibration cylinders were calibrated against the DACOM NOAA cylinders, the accuracy determined from the uncertainty in the NOAA cylinders should have the

https://doi.org/10.5194/egusphere-2026-1686
Preprint. Discussion started: 10 April 2026

same effect on the accuracy of our calibration cylinders. Therefore, for the combined uncertainty we only include the precision of DACOM and the total uncertainty of the MGA^3, which includes the precision of each data point and the uncertainty of our own cylinders an.

To quantify the agreement between the MGA^3 measurements and DACOM, we calculate the fraction of data points that overlap within the combined uncertainty of both instruments which is summarized in Table 3. In Figure 6(a) for the 2024-03-25, the difference between DACOM and v1-β-off (orange line) is already very small with $74.5\,\%$ of data overlapping between the two instruments. This indicates that the behavior of H_2O of the water laboratory experiment is actually close to the mean behavior for all ASIA-AQ flights (dashed black line, Figure 5) and therefore to the behavior during this flight. This is indicated by the differences for v1-β-off-DLH (green line) which show only smaller deviations compared to v1-β-off due to the application of the DLH-correction ($74.4\,\%$ overlap with DACOM). The differences for v2, however show a drift with increasing H_2O mole fractions with $60.8\,\%$ of data overlapping DACOM. In particular, for H_2O values above $1.5\,\%$ or $15000\,\mathrm{ppm}$ the differences between DACOM and v2 are larger than the combined uncertainties. A reason for the drift can be water dependencies found in the pressure regulator used in the MGA_3 which is replaced by an updated regulator in the newer models (personal communication with Oleg Aseev). In Figure 6(b) and (c), the differences for v1-β-off show deviations greater than $1\,\mathrm{ppb}$ compared to DACOM. The overlap of the data is $53.1\,\%$ and $70.1\,\%$, respectively. This can be explained by the indicated changes in the sensitivity of the MGA^3-H_2O measurements as discussed in Chapter 3.3. When corrected with DLH, however, the resulting v1-β-off-DLH corrected data overlaps within $79.4\,\%$ and $82.3\,\%$ with DACOM data and the deviations for larger H_2O values decrease. For the 2024-03-21 and 2024-03-18 in v2 the same trends are found in Figure 6(b) and (c) as for the 2024-03-25 shown in Figure 6(a).

There are several possible reasons that the percentages of overlapping data with DACOM do not reach higher values than 82%. First, of course, the two instruments are not identical and react inherently different to changes in the measured species especially due to the different setups (Nafion-drier, pump, mass flow, etc.). Second, DACOM used one additional calibration cylinder and calibrates every $4\,\mathrm{min}$ while our setup uses only two cylinders for calibrations every $10\,\mathrm{min}$, making our instrument potentially more prone to changes in sensitivity compared to DACOM. Third, it could be that the distance of the inlets for the two instruments of about $20\,\mathrm{m}$ leads to the sampled air by both instruments not being identical. In the case of v1-β-off-DLH, a last reason could be that the mean behavior of H_2O for all flights in Figure 5(a) (dashed black line) correcting the laboratory experiment does not represent the actual true behavior. This could also explain the slight negative trend in N_2O from lower to higher H_2O values.

We conclude that the v1-β-off approach could be improved by the additional DLH correction resulting in the v1-β-off-DLH approach. The newer v2 version shows shows a significant drift for growing H_2O mole fractions but matches DACOM until $1.5\,\%$ or $15000\,\mathrm{ppm}$ H_2O within the uncertainties. However, it does not need an additional adjustment with DLH data or data from other instruments as v1-β-off-DLH.

https://doi.org/10.5194/egusphere-2026-1686
Preprint. Discussion started: 10 April 2026

Table 4. Contribution of the N_2O-precision, H_2O-precision, calibration and water vapor correction procedure to the total squared uncertainty for the v1-β-off N_2O data in percentages.

	mean / %	min-max / %
precision N_2O	93.25	$88.05 - 97.27$
precision H_2O	4.49	$1.55 - 7.53$
calibration	0.04	$0.01 - 0.1$
water vapor correction	2.22	$0.9 - 4.8$

3.5 N_2O precision, noise and uncertainty

In Section 2.5, we explained the possibility of changing the-β setting and how it influences the fitting process. An advantage from the deactivation of the β is, that the fitting software has one less parameter that has to be accounted for in the fitting process, leading to less noise in the retrieved mole fractions.

Therefore, we compare the precision of 14 ASIA-AQ flights refitted with the approaches v1-β-off, v1-β-off-DLH and v2. We determine the in-flight precision by calculating the mean of the precision values for each flight, obtained by propagating the standard deviations of all calibration time windows within the given flight, such as the one in Figure 2. The mean N_2O precision for both the v1-β-off-DLH version and the v2 version is about $42\,\% \pm 4\,\%$ lower than for the v1-β-off version. The lowest determined in-flight precision for a flight at ASIA-AQ with the v1-β-off-DLH version was approximately $0.17\,\mathrm{ppb}$.

Further uncertainties arise from the calibration and the water vapor correction of the data. We summarize the uncertainty budget in Table 4 in percentages according to the contribution to the total uncertainty. After propagating the precision of the N_2O measurements through the calibration Equation (3) and the water vapor correction Equation (17) we find, that in the mean across flights the precision of N_2O contributes about $93\,\%$ to the squared total uncertainty. The H_2O-precision, usually in the range of approximately $0.01\,\mathrm{vol}\%$, contributes approximately $4.5\,\%$, the calibration procedure about $0.05\,\%$ and the water vapor correction procedure about $2.2\,\%$ to the total squared uncertainty. However, in this calculation, we assume that the uncertainties of the NOAA-cylinders used for cross calibrating our own calibration cylinders are 0 and therefore only apply the uncertainties of our calibration cylinders which are $< 0.1\,\mathrm{ppb}$ using standard errors. The squared uncertainty of the H_2O measurements itself also increases by roughly $40\,\%$ after applying the DLH-correction to the ASIA-AQ data.

The precision depends crucially on the optics alignment. Usually, we recognize a misalignment by a drop in the detected laser intensity, by worsened residuals when fitting the spectra or by worsened precision values compared to previous measurements which all can be corrected again by realigning the mirrors. The mirrors directing the laser beams into the measuring cell can misalign when the instrument experiences heavy shocks. We also experienced a misalignment after transporting the instrument with a van over several hours on the highway. Onboard the Cessna at the GHGMon campaign we did not experience any clear misalignment over the course of roughly 50 flight hours (including transfer flights). Onboard the DC-8 at ASIA-AQ, we did not experience any clear changes in the alignment either for about 90 flight hours. In South Korea, even after warming up

https://doi.org/10.5194/egusphere-2026-1686
Preprint. Discussion started: 10 April 2026

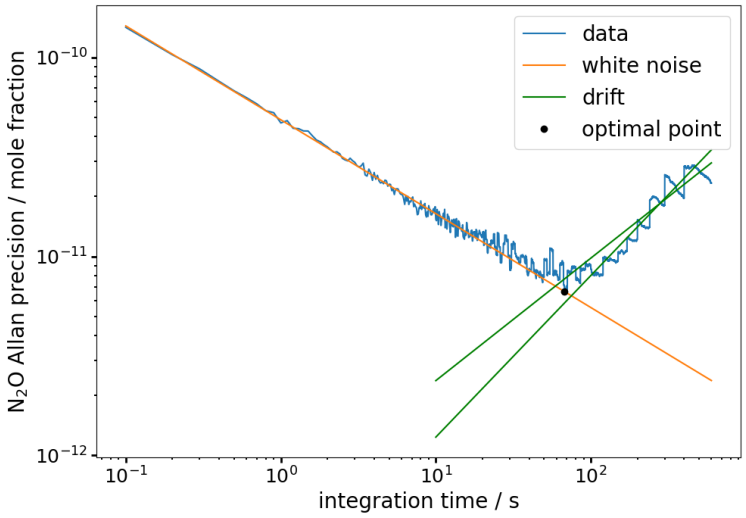

Figure 7. Allan Precision for N_2O. Values along the orange line are considered white noise. The green lines show the minimum and maximum range for drift behavior. The optimal integration time τ after which the drift sets in is shown with the black dot at $\tau = 67\,\mathrm{s} \pm 8\,\mathrm{s}$.

the device for 1-3 hours from temperatures slightly above the freezing point over night to $25\,^{\circ}\mathrm{C}$ in the optics compartment of the instrument we could not see any significant changes to the alignment and precision. However, after the transfer flight from South Korea to Thailand, a clear misalignment in the optics worsening the precision of the instrument by about 50-100 % for the last four campaign flights. The optics could be realigned again in the laboratory after the campaign. The source of the misalignment could have multiple reasons, e.g, heavier shocks than usual while landing, but we could not identify any specific cause. In general, we realign the optics before every campaign for optimal data quality. Because of a possible misalignment, we recommend to built in the MGA^3 in the top of a rack to have easier access to the mirrors while doing flight tests.

We conclude that the v1-β-off-DLH and v2 versions give a better precision for the data than the v1-β-on version. However, for the v1-β-off-DLH version to work, we have to determine an empirical water correction as described in Chapter 3 whereas version v2 works with no additional data refinement after the mole fraction retrieval. The instrument is stable in regards of its optical alignment over whole campaigns with about 50 flight hours and longer. Nonetheless, we recommend a realignment of the optics before every campaign for optimal data quality.

4 Stability of the DLR airborne MGA^3 system

4.1 Allan Precision and calibration frequencies

In this section, we determine the stability of the MGA^3-N_2O via its Allan precision according to Werle et al. (1993), as can be seen in Figure 7. We calculate the Allan precision from a $20\,\mathrm{min}$ time series of a measured calibration gas in the laboratory on ground and discuss the optimal calibration times and frequencies for the in-situ measurement. The range of white noise can

https://doi.org/10.5194/egusphere-2026-1686
Preprint. Discussion started: 10 April 2026

Table 5. Allan Precision for different integration times τ in Figure 7. The optimal integration time is at 67 s. The values for $\tau = 1\,\mathrm{s}$, 200 s are slightly higher than the values given by the manufacturer.

integration time τ	calculated (ppb)	manufacturer values (ppb)
@0.1 s	0.15	
@1 s	0.05	0.03
@10 s	0.017	
@67 s	0.007	
@100 s	0.009	
@200 s	0.015	0.01

be found along the orange line. The two green lines show the maximum and the minimum slope where the behavior of the instrument shows a drift. Based on this, the optimum integration time $\tau = 67\,\mathrm{s} \pm 8\,\mathrm{s}$ was determined by calculating the mean of the times between the intersects of the green and orange lines. In Table 5, the result for a set of integration times τ can be seen, including two values that were given by the manufacturer. Our self-determined values are comparable to the manufacturer values but are slightly higher. Therefore, the data should be calibrated about every 67 s to avoid any drift in the data. However, this would lead to a duty cycle of about 63 % leading to a high and expensive calibration gas consumption. As a trade-off between data quality, gas consumption, and data acquisition, we chose to calibrate for 40 s in total every 10 min leading to a duty cycle of about 94 %, as we already saw in Figure 2 in an example from the ASIA-AQ campaign. The calibration time windows show stable behavior within their respective 20 s and, in combination with the high cell exchange rate and after our experience at the GHGMon and ASIA-AQ campaigns, we suggest even shorter periods than 20 s for the high and low standards in future flights, further improving the duty cycle of our our system.

4.2 Dependency on cabin pressure

As previously noted, the DC-8 aircraft has a pressurized cabin while the DLR Cessna aircraft is unpressurized. In the DC-8 the cabin pressure data are provided by the DC-8 Meteorological and Navigation Facility Instrumentation (MetNav). As a proxy for the cabin pressure in the Cessna, we use the static pressure measurement provided by the meteorological sensor package (METPOD). Previously, Pitt et al. (2016) have shown cabin pressure dependencies in their data resulting in deviations of several ppb for pressures ranging from about 1000 hPa down to 800 hPa, which were corrected by a pressure differentiated calibration procedure. However, with this procedure the data is filtered by a condition where the influence of pressure is small, leading to high losses in the amount of data. Gvakharia et al. (2018) also showed deviations in N_2O within a similar pressure range. These deviations were accounted for by frequent calibrations.

To study the potential effect of cabin pressure on the measurement quality, we measured calibration gas during a specific descent of the DLR Cessna for about 8 min covering a pressure change from 820 hPa to 880 hPa. To study the effect onboard the NASA DC8, we specifically asked to actively lower the cabin pressure between 840 hPa and 760 hPa within 8 min. Figure 8

https://doi.org/10.5194/egusphere-2026-1686
Preprint. Discussion started: 10 April 2026

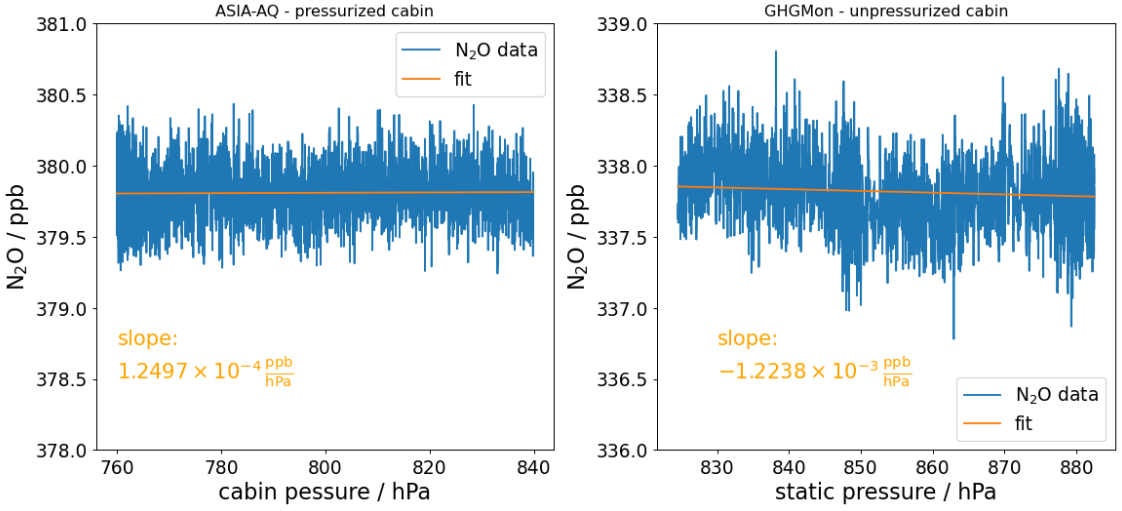

Figure 8. On the left, N_2O calibration gas measurements are plotted against the cabin pressure of the NASA DC8. The pressure of the pressurized cabin was actively reduced from $840\,\mathrm{hPa}$ to $760\,\mathrm{hPa}$ within $8\,\mathrm{min}$. The slope of the fit function shows no significant drift in N_2O. On the right we see the N_2O calibration gas measurements plotted against the static pressure as a proxy for the cabin pressure, because the cabin of the DLR Cessna is not pressurized. During a descent within $8\,\mathrm{min}$ the static pressure increased from $820\,\mathrm{hPa}$ to $880\,\mathrm{hPa}$. The slope shows a significant drift for pressure changes of more than roughly $150\,\mathrm{hPa}$, which would be higher than the precision of the instrument $0.17\,\mathrm{ppb}$. However, the behavior seems to be less stable so that the drift does not seem to be connected to changes in cabin pressure alone.

shows the retrieved mole fractions of the sampled calibration gas, once plotted against the cabin pressure of the DC8 and once against the static pressure for the DLR Cessna during the descent. For the ASIA-AQ data no obvious dependencies on the cabin pressure can be identified. The data seems to be stable, as can be seen from the fit of the data with a slope of $1.2497 \times 10^{-4}\,\frac{\mathrm{ppb}}{\mathrm{hPa}}$. For a pressure change in the range of $1000\,\mathrm{hPa}$, the resulting drift would still almost be within the uncertainty/precision of $0.19\,\mathrm{ppb}$ of the instrument for these $8\,\mathrm{min}$. However, for the GHGMon flight with the unpressurized cabin a less stable behavior with a standard deviation of $0.24\,\mathrm{ppb}$ can be seen, which is higher than the determined precision for this flight with $0.17\,\mathrm{ppb}$. The fit function shows a slope of $-1.2238 \times 10^{-3}\,\frac{\mathrm{ppb}}{\mathrm{hPa}}$, but it does not show a clear linear behavior which would indicate a clear dependency on the cabin pressure alone.

We conclude that the measurements from the unpressurized cabin are less stable but are probably not solely linked to cabin pressure changes alone. Nonetheless, we recommend for both a pressurized and unpressurized cabin to sample calibration gas before and after each relevant ascent or descent in a profile to minimize any drift.

4.3 Dependency on roll and pitch angle

In this section, we analyze if changes in the roll and pitch angle of the aircraft influence the measurements of the MGA[3]. For example, Pitt et al. (2016) introduced a quality flag for their data for roll angles over $10\,°$, which caused deviations in the

https://doi.org/10.5194/egusphere-2026-1686
Preprint. Discussion started: 10 April 2026

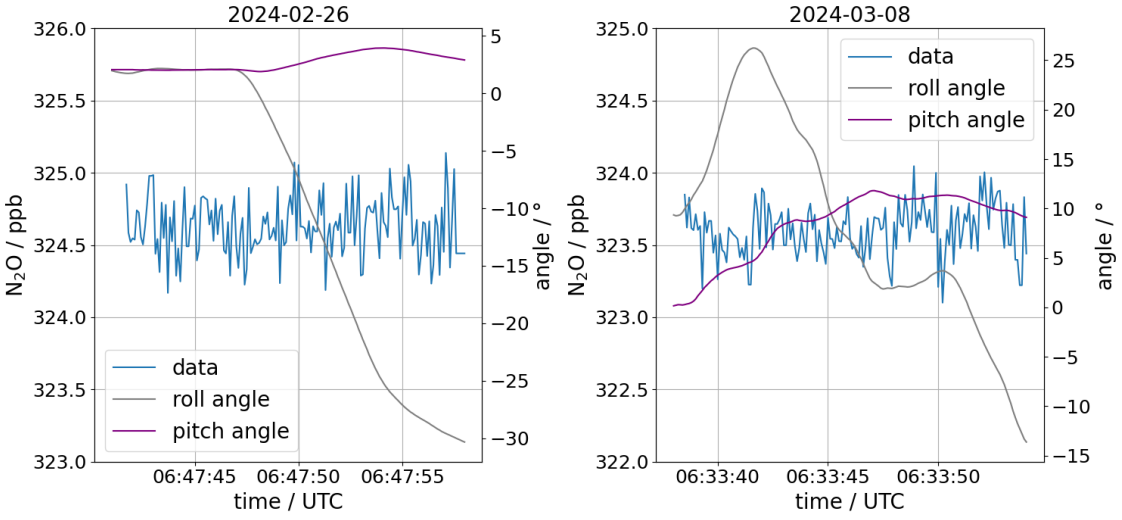

Figure 9. Calibration gas measured in-flight at the ASIA-AQ campaign during changing roll and pitch angles on the 2024-02-26 and the 2024-033-08 in South Korea. On the 2024-02-26 we flew a left turn with a roll angle up to $-30\,°$ while the pitch angle was almost constant. On the 2024-03-08 we were ascending with a pitch angle of up to $12\,°$ while changing from a right turn to a left turn with roll angles from $25\,°$ to $-15\,°$. In both flights no dependencies that are larger than the respective noise of the measurements could be found.

measurements due to the centrifugal force acting on the alignments in the laser setup. The roll angle describes the rotation of the aircraft around its longitudinal axis (nose to tail) respective to its initial horizontal position of the wings (positive values: clockwise rotation looking forward) and the pitch angle describes the the rotation of the aircraft around its lateral axis (wing tip to wing tip) respective to its initial horizontal position (positive values: nose up). The roll and pitch angle data were provided by the DC-8 MetNav. The minium and maximum reached values for the roll angle during all flights at the ASIA-AQ campaign were $-36\,° \pm 4\,°$ to $36\,° \pm 4\,°$ and for the pitch angle $-8\,° \pm 2\,°$ to $15\,° \pm 2\,°$.

In Figure 9, we plotted data of $15\,\mathrm{s}$ from two calibration time windows from the flights on the 2024-02-26 and 2024-03-08 against the roll and the pitch angle of the aircraft. In (a) and (b) we cannot see any clear dependency of the measurements on the angles that are larger than the noise or precision of our measurements.

5 Case Studies and example measurements

In this section, we present calibrated and water vapor (v1-β-off-DLH) corrected N_2O measurements from the ASIA-AQ campaign. The goal of the campaign is to better understand the air quality in Southeast and East Asia through airborne in-situ measurements that later on can be used for validating models and satellite data (Crawford et al., 2025). The general approach was to fly the same pattern specifically designed for each country repeatedly for multiple flights to acquire data for large horizontal ranges within the PBL. The flight patterns were repeated two to three times per flight with frequent profiles to scan the whole PBL at different day times. Within a pattern, the profiles were flown at the same locations, as far as possible. With

https://doi.org/10.5194/egusphere-2026-1686
Preprint. Discussion started: 10 April 2026

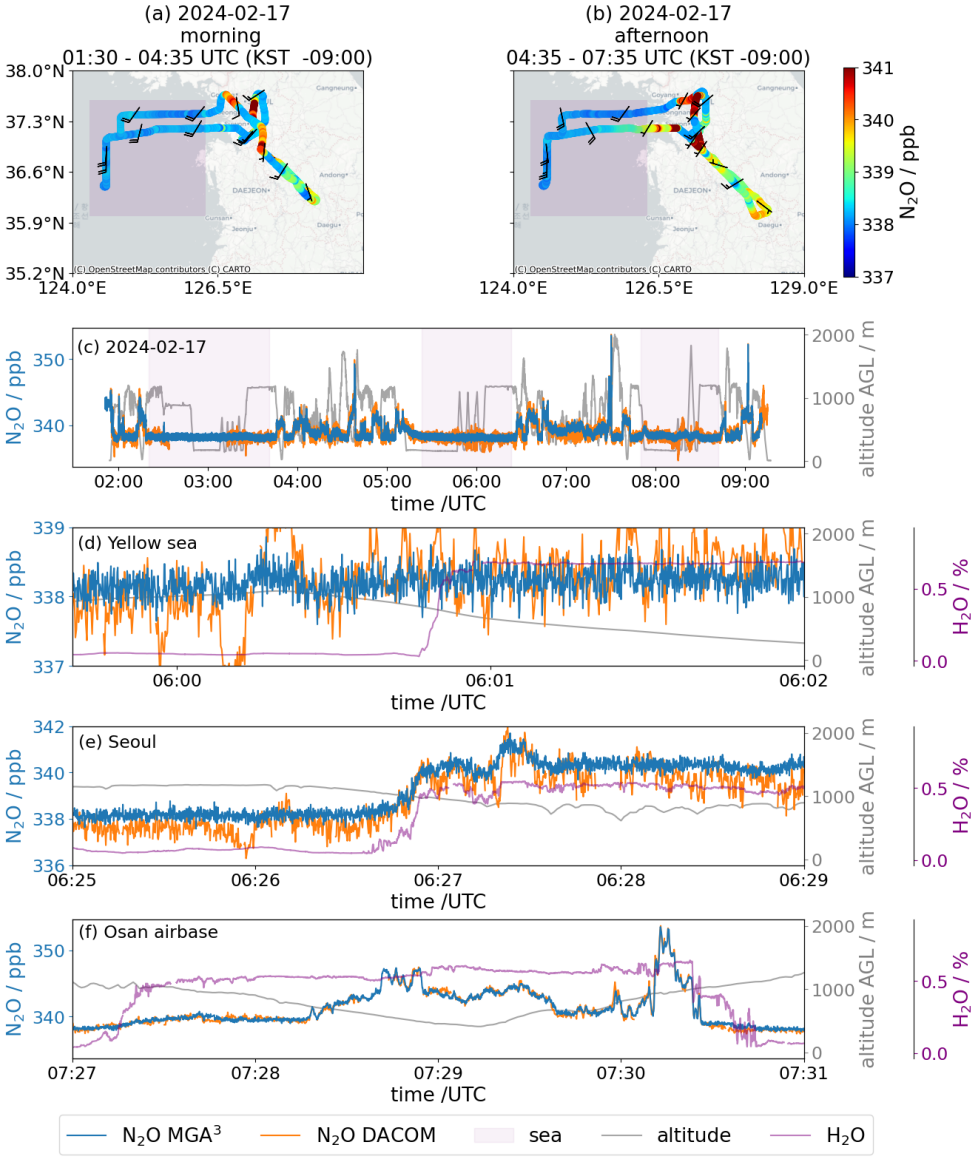

Figure 10. Comparison of color coded N_2O data measured by the MGA[3] in the morning in Figure (a) and in the afternoon in Figure (b) of the same flight in South Korea on the 2024-02-17. Panel (c) depicts the time series for the whole flight measured by the MGA[3] (10 Hz, precision: 0.18 ppb) and DACOM (5 Hz, precision: 0.3 ppb) and the altitude above ground level showing the frequent ascents and descents. The purple shaded areas show the flight paths over the yellow sea in (a) and (b), where we measured background concentrations of about 338 ppb in N_2O. Figure (d) shows data from the afternoon over the Yellow sea where we entered the PBL. The change in water vapor mole fraction while entering does not show any effect on the water vapor corrected v1-β-off-DLH data and the air seems to be clean enough to show no changes in N_2O compared to the background measurements outside the PBL. Figure (e) shows data while entering the PBL over Seoul where enhancements in N_2O can be seen. Figure (f) shows enhancements of up to 16 ppb in N_2O between Pyeongtaek and Anseong approaching Osan Airbase which are in good comparison with the DACOM measurements.

https://doi.org/10.5194/egusphere-2026-1686
Preprint. Discussion started: 10 April 2026

this, we acquired a N_2O data set with about $100\,h$ of combined data measured at $10\,Hz$ for the regions of Luzon (Northern Philippines), Taiwan, South Korea and Thailand in the winter of 2024. GPS-data and altitude above ground level (AGL) were provided or deduced from the measurements of the DC-8 MetNav. The wind measurements at flight altitude were provided in $20\,Hz$ by the Meteorological Measurement System (MMS) (Scott et al., 1990) which is used on multiple NASA aircraft.

Figure 10 presents an example flight from the campaign in South Korea on the 2024-02-17 and shows the variability of N_2O data as observed on large horizontal scales. Figure 10(a) and (b) show the flight tracks for the morning and afternoon flights, respectively, color coded by measured N_2O. The wind barbs indicate southerly to southwesterly winds over the whole flight. In the afternoon (Figure 10(b)), slightly higher enhancements can be found than in the morning (Figure 10(a)). Especially, the southerly flight path leading west from the land to the sea shows higher enhancements in the afternoon than in the morning. Those enhancements could be caused by the coal fired KOEN Yeonheung Power Plant on Yeonheung island but also by transport from land due to the mainly southerly winds in the afternoon. The correct source attribution is beyond the scope of this work and will be part of an upcoming study. Figure 10 (c) shows the time series of the whole flight with a duration of about $7\,h$ as measured by the MGA[3] ($10\,Hz$, precision: $0.17\,ppb$) and by DACOM ($5\,Hz$, precision: $0.3\,\%$). The grey lines represent the flight altitude above ground level (AGL), showing the frequent level changes and vertical profiles between $0\,m$ and $2000\,m$. Over the Yellow Sea west of South Korea, indicated by the purple shaded areas, the N_2O background mole fraction is relatively constant at about $338\,ppb$. Here, no significant differences within and outside the PBL are observed for N_2O, as shown in more detail in Figure 10(d). A change in H_2O of about $0.7\,\%$ is observed when entering the PBL at $\sim 900\,m$ during a descent, while the water vapor corrected N_2O values remain at the same level. The figure also illustrates the better precision and stability of the DLR-MGA3 in comparison to the DACOM instrument. In contrast, much higher mole fractions with enhancements of about $3\,ppb$ compared to the background were measured when entering into the PBL over Seoul (Figure 10(e)). Finally, Figure 10(f) illustrates the general good comparison between the MGA[3] data and the DACOM data over larger ranges in N_2O mole fractions, with enhancements of up to $16\,ppb$ as measured during a vertical profile taken close to the Osan Airbase.

Using the frequent profiles, we can compare the vertical distribution of N_2O for different regions and also compare it to other species. In the following example, we use NH_3 for comparison, since the agricultural sector is the main anthropogenic source for both species (Behera et al., 2013). The NH_3 was measured by the Los Gatos Research Ammonia Analyzer - Trace (LGR-AAT) (1σ,$0.1\,s$: $0.7\,ppb$) operated by the Hankuk University of Foreign Stuies (HUFS) and the National Institute of Environmental Research (NIER) in South Korea. In Figure 11(a), (b) and (c), by using the data from all flights for South Korea and Thailand respectively and a single flight for Taiwan, we calculate the 50th and 90th percentile for N_2O (blue and cyan) and NH_3 (red and orange) for $100,m$ bins with. Each bin has about >1000 values except for Taiwan with >100. Due to the warmer temperatures in Thailand and Taiwan compared to South Korea, we generally had to fly higher to scan the PBL completely. For the 50th percentile of N_2O, slightly higher values of $1\text{-}2\,ppb$ in Thailand and in Taiwan than in South Korea can be seen for AGL flight altitudes below $1500\,m$ and $1000\,m$, respectively. For the 90th percentile below $1000\,m$ in Thailand, higher values of up to $4\,ppb$ in N_2O compared to South Korea and up to $2\,ppb$ higher than in Taiwan can be seen. One reason for the higher N_2O values in Thailand compared to South Korea could be the impact of lower temperatures on agriculture in South Korea during February. In general, a reason for the high N_2O measured over Thailand could be, that we flew over Central Thailand over

https://doi.org/10.5194/egusphere-2026-1686
Preprint. Discussion started: 10 April 2026

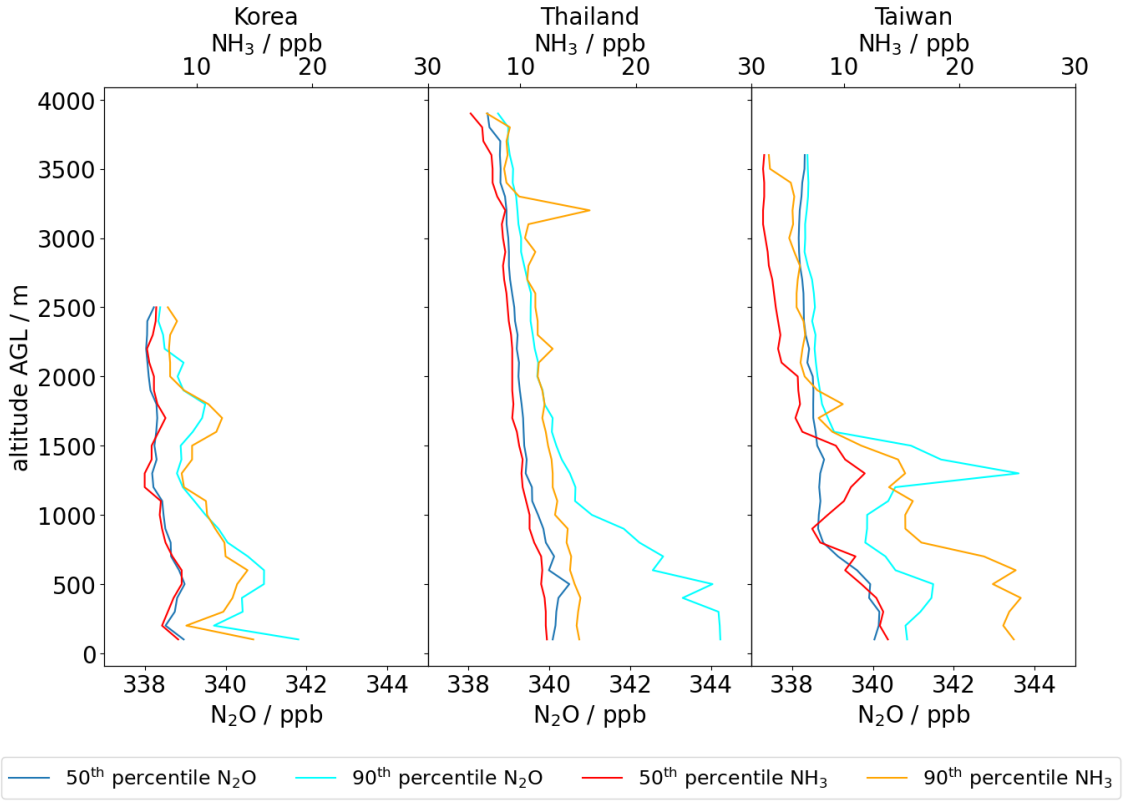

Figure 11. The 50th and 90th percentile of N_2O and NH_3 for South Korea, Thailand and Taiwan. For each country data from all flights are taken to calculate the percentile, except for Taiwan, where we have data from one flight only. In Thailand and Taiwan had to fly higher than in Korea to get out of the PBL due to higher ambient temperatures. In Korea N_2O and NH_3 show similar behavior. In Thailand the N_2O shows an increase for altitudes below $1500\,\mathrm{m}$ due to a rain event in one flight, after which the N_2O emissions were higher over agricultural areas. In general Thailand shows higher enhancements in the PBL for N_2O due to the higher agricultural activities in this region. In Taiwan an increase in N_2O around $1500\,\mathrm{m}$ altitude can be seen, which was measured at a technology park at Tainan with manufacturing plants by TSMC.

a plain stretching from Bangkok to Northern Thailand where agriculture is very prominent and concentrated over thousands of square kilometers. Additionally, on the flight of the 2024-03-21, there was a rain event after which N_2O emission rose in general with enhancements of up to $14\,\mathrm{ppb}$ in that area dominating the higher N_2O values for the 90th percentile in Thailand. Those enhancements were measured mainly in agricultural areas. In Taiwan, in the 90 percentile a high enhancement of up to $6\,\mathrm{ppb}$ can be seen compared to the background around an altitude of 1000-$1700\,\mathrm{m}$. These enhancements with maximum values of $15\,\mathrm{ppb}$ originate mainly from the overflights over a technology park divided between the Anding, Shanhua and Xinshi Districts of Tainan where several plants of semiconductor and chip manufacturers like TSMC are located. Additionally, the technology park is surrounded by agricultural fields and contains a waste water treatment facility making this area complex

https://doi.org/10.5194/egusphere-2026-1686
Preprint. Discussion started: 10 April 2026

for source attribution. For NH_3, we can see that the 90th percentile in South Korea shows structures similar to those of N_2O. In Taiwan, first, the 50th percentile of NH_3 and the 90th percentile of N_2O seem to match at the altitudes around $1500\,\mathrm{m}$, but then the 90th percentile NH_3 seems to diverge more to higher values for altitudes below $1500\,\mathrm{m}$. For Thailand, NH_3 does not seem to correlate with the N_2O percentiles, especially not with the 90th percentile, although these enhancements in N_2O originate mainly from agricultural regions.

In an already conducted study by Waldmann et al. (2026) at the GHGMon campaign 2023 in the Netherlands, our MGA^3 was used for a N_2O eddy covariance study, calculating N_2O fluxes. For a comparison, we applied the same method for specific, representative flux legs across one research flight, once with the v1-β-off water correction and once with the v2 correction. In the comparison, we could find that the relative difference between the results was around $3\,\%$ which is an order of magnitude smaller than the typical relative flux errors reported by Waldmann et al. (2026). Hence, for this instrument setup, we cannot find any significant difference in the influence of the water vapor correction approaches on the calculated eddy covariance fluxes.

6 Summary and Conclusions

In this paper, we evaluate a measurement system for fast ($10\,\mathrm{Hz}$) airborne N_2O measurements. The core of the system consists of a commercial QCLAS, the Multicompound Gas Analyzer (MGA) from MIRO Analytical AG (Switzerland). The system was successfully deployed twice: during the 2023 GHGMon campaign aboard the DLR Cessna with an unpressurized cabin in the Netherlands, and during the 2024 ASIA-AQ campaign aboard NASA's DC8 with a pressurized cabin over South Korea, Thailand, the Philippines, and Taiwan. The system is calibrated using a two-point calibration every $10\,\mathrm{min}$, with a high and low standard gas for approximately $40\,\mathrm{s}$ in total, resulting in a duty cycle of about 94%. Under this setup, the measuring cell is fully flushed with calibration gas in under $1\,\mathrm{s}$, indicating that the duty cycle could be further increased by reducing the calibration duration.

We operate the instrument in the β-deactivated mode, in which the fitting software freezes the last value used for the width of the spectral profile. By reducing the number of adjustable parameters, this mode decreases the data noise by about $42\,\%$ compared to the default β-activated setting. However, because the spectral profile widths are strongly influenced by the highly variable H_2O in the PBL, cross-dependencies on H_2O remain observable in the data.

To correct H_2O dependencies in both the β-deactivated and the β-activated mode, arising from dilution, line broadening, and other spectroscopic effects, we derived an empirical water vapor correction from laboratory experiments. We further observed that, from flight to flight, the H_2O measurements show differences relative to NASA's DLH measurements. This is likely due to the inability to perform a two-point calibration of the MGA$_3$ H_2O measurements, as our calibration gases are dry standards. To improve the H_2O correction, we therefore calibrate the MGA^3 H_2O measurements against the DLH data leading to the water vapor corrected version of the MGA data, namely the v1β-off-DLH. Also, we tested a new version of the MGA$_3$ fitting software, namely v2, that includes a water vapor correction based on the same laboratory experiments. For H_2O values up to $15000\,\mathrm{ppm}$, v2 performs comparably to the v1β-off-DLH, showing similar precision (approximately $0.17\,\mathrm{ppb}$. The v1β-off-DLH data compares well with N_2O measurements from NASA's DACOM measured simultaneously with our system at

https://doi.org/10.5194/egusphere-2026-1686
Preprint. Discussion started: 10 April 2026

the ASIA-AQ campaign even up to 30000 ppm H_2O. In example data from ASIA-AQ we show that clear differences within large horizontal and vertical scales can be distinguished between different regions with high humidity. We also compare the two approaches using GHGMon campaign data (Waldmann et al., 2026) to calculate eddy covariance fluxes, but found no significant difference in the resulting fluxes.

We did not observe clear dependencies of the measurements on the aircraft's roll and pitch angles, nor cabin pressure, while sampling calibration gas. However, on the DLR Cessna with its unpressurized cabin, the measurements were generally slightly less stable.

We conclude that the presented instrumental setup enables fast and precise airborne N_2O measurements, suitable for eddy covariance flux estimates and for deployment in highly humid tropical regions.

Data availability. The data are available from the author upon request. All of the ASIA-AQ campaign data is available on the archive: https://www-air.larc.nasa.gov/cgi-bin/ArcView/asiaaq (https://doi.org/10.5067/SUBORBITAL/ASIA-AQ/DATA001, ASIA-AQ Science Team, 2024)

Appendix A: Dependency of absorption coefficient α on water vapor H_2O

The absorption coefficient α is retrieved from the HITRAN Database 2016 (Gordon et al., 2017). According to the official HITRAN website at https://hitran.org/docs/definitions-and-units/ (Gordon et al., 2022) α is defined as:

$$\alpha(\nu,T,p) = S_{ij}(T)\, f(\nu,\nu_{ij},T,p)\,, \tag{A1}$$

where S_{ij} is the intensity of a spectral line for a single molecule for the transition between two states i and j, f the Voigt profile and ν_{ij} the wavenumber of the spectral line transition in vacuum. The Voigt profile further consists partially of a normalized Lorentz profile f_L defined as:

$$f_\mathrm{L}(\nu,\nu_{ij},T,p),= \frac{1}{\pi}\frac{\gamma(p,T)}{\gamma(p,T)^2+\left[\nu-\nu_{ij}^*(p)\right]^2}\,. \tag{A2}$$

Here ν_{ij}^* is the pressure shift corrected wavenumber ν_{ij} and γ is the Lorentzian Half-Width-Half-Maximum (HWHM) width of the line shape. In the case of pressure broadening on the observed species induced by air, water vapor and the species itself, the resulting width γ is defined as (Kostinek et al. (2019), https://hitran.org/docs/definitions-and-units/):

$$\gamma(p,T) = \left(\frac{T_\mathrm{ref}}{T}\right)^{n_\mathrm{air}} \left(\gamma_\mathrm{air}(p_\mathrm{ref},T_\mathrm{ref})\,(p-p_\mathrm{self}-p_{\mathrm{H_2O}}) + \gamma_\mathrm{self}(p_\mathrm{ref},T_\mathrm{ref})p_\mathrm{self} + \gamma_{\mathrm{H_2O}}(p_\mathrm{ref},T_\mathrm{ref})p_{\mathrm{H_2O}}\right)\,. \tag{A3}$$

Here γ_air, γ_self and $\gamma_{\mathrm{H_2O}}$ are the HWHM induced by the partial pressures p_air, $p_{\mathrm{H_2O}}$ and p_self of air, water vapor and the species itself at a reference temperature $T_\mathrm{ref} = 296\,\mathrm{K}$ and pressure $p_\mathrm{ref} = 1\,\mathrm{atm}$.

Specifically for the N_2O absorption line used in our MGA[3], the HITRAN data base shows that H_2O has a higher broadening effect than air (=nitrogen (N_2), oxygen (O_2)) and N_2O itself with $\gamma_{\mathrm{H_2O}} = 0.1308$, $\gamma_\mathrm{air} = 0.0701$ and $\gamma_\mathrm{self} = 0.085$ (Gordon

https://doi.org/10.5194/egusphere-2026-1686
Preprint. Discussion started: 10 April 2026

et al., 2022). The difference between γ_{self} and $\gamma_{\mathrm{N_2O}}$ has important implications on the spectral line width. While the global background concentration of N_2O in the troposphere is in the range of about $338\,\mathrm{ppb}$, H_2O mole fractions lie between $1\,\mathrm{ppm}$ to $10\,\mathrm{ppm}$ even in the dry stratosphere, but can get specifically high in regions such as the tropical boundary layer (up to $30000\,\mathrm{ppm}$, which is 4 to 5 orders of magnitudes higher than for N_2O. With this, we can simplify equation (A3) for measurements in the troposphere to:

$$\gamma(p,T) = \left(\frac{T_{\mathrm{ref}}}{T}\right)^{n_{\mathrm{air}}} \left(\gamma_{\mathrm{air}}(p_{\mathrm{ref}},T_{\mathrm{ref}})\,(p - p_{\mathrm{H_2O}}) + \gamma_{\mathrm{H_2O}}(p_{\mathrm{ref}},T_{\mathrm{ref}})p_{\mathrm{H_2O}}\right). \tag{A4}$$

Therefore, we assume the width γ of our measured line spectra to be mainly dependent on water vapor for atmospheric measurements in the troposphere, assuming that T and p are constant in the cell.

Appendix B: N_2O Eddy Covariance GHGMon

Waldmann et al. (2026) used the same MGA^3 as presented in our study to conduct airborne eddy covariance flux measurements in the course of the GHGMon (Greenhouse Gas Monitoring) campaign 2023 in the Netherlands. Precise high-frequency GHG measurements without interference from water vapor related effects are a prerequisite for robust flux measurements, as water vapor mole fractions are often quite distinct between turbulent updrafts and downdrafts, potentially falsifying GHG measurements if not properly corrected. In order to investigate the extent to which different water vapor correction approaches affect flux measurements, we applied both, the v1-β-off water correction and the v2 correction to specific, representative flux legs across one research flight of the study of Waldmann et al. (2026).

In Figure B1(a) and (b), we can see the vertical wind measurements and the H_2O measurements of the METPOD system on the DLR Cessna from a flight in Friesland on 21 June 2023. Both show high-frequency fluctuations, typical during fair-weather turbulent conditions, which in turn are fundamental for applying the eddy covariance methodology. In Figure B1(c), we see the MGA^3-N_2O measurements for the v1-β-off and v2 water correction approaches, similarly showing high-frequency variability expected in the turbulent PBL. In Figure B1(d), the calculated eddy covariance fluxes are shown as time series for the two retrieved mole fractions from (c), calculated according to the procedure presented in **?**. The mean value for the fluxes over the given time frame is slightly higher for the fluxes with the v2 water correction ($0.36\,\mathrm{g\,m^{-2}s^{-1}}$) compared to the fluxes with the v1-β-off water correction ($0.33\,\mathrm{g\,m^{-2}s^{-1}}$), which translates to a relative difference of $9\,\%$. This difference is expected, given the drift in N_2O corrected according to v2, with increasing H_2O (see Section 3.4). However, the relative difference ($9\,\%$) is approximately 1 order of magnitude smaller than typical relative flux errors reported in **?**, which range between 30-100 %, which are superimposed as error bars for the v1-β-off fluxes in Figure B1(d).For both corrections, we computed the limit of detection of N_2O fluxes, which was found to be slightly higher for the v2 water correction ($0.028\,\mathrm{g\,m^{-2}s^{-1}}$ compared to $0.017\,\mathrm{g\,m^{-2}s^{-1}}$ for v1-β-off. Given that the differences in fluxes derived with both water vapor corrections is one order of magnitude smaller than typical flux errors, we conclude that the choice of water correction approaches is not a limiting factor for the quality of such flux measurements, but have to be considered when corresponding systems should be improved or small fluxes close to the detection limits are to be measured. We note explicitly that these conclusions are only valid for

https://doi.org/10.5194/egusphere-2026-1686
Preprint. Discussion started: 10 April 2026

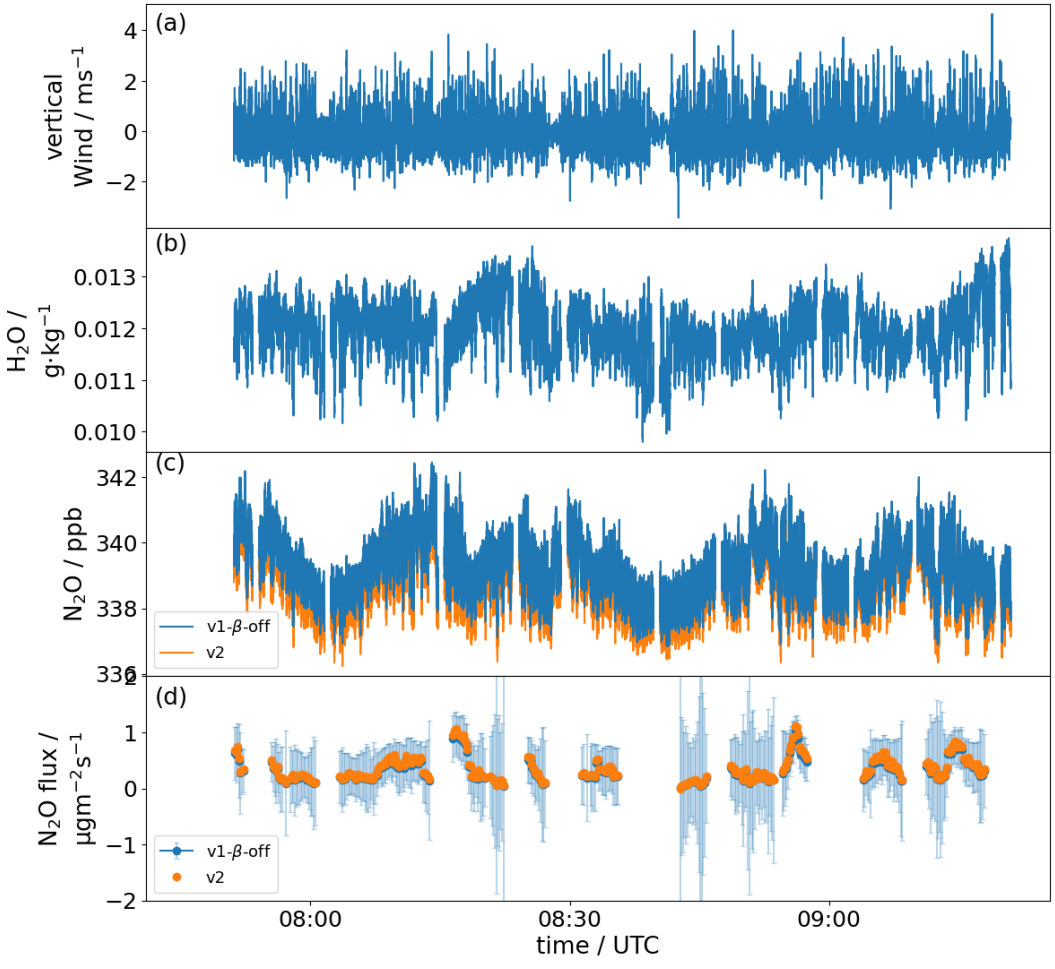

Figure B1. Panel (a) presents vertical wind measurements from a flight on 21 June 2023 in the Netherlands. Panel (b) shows corresponding H_2O measurements. Panel (c) shows the water vapor corrected N_2O measurements, once retrieved with v1-β-off and once with v2. Subplot (d) shows the calculated eddy covariance fluxes from the respective time series in Figure (c), error bars depicting the uncertainty associated with the flux computation.

the comparison of the water vapor corrections presented within this work, and do not represent differences in fluxes calculated with mole fraction measurements with and without water vapor correction.

Author contributions. LK wrote the paper, did the analysis and prepared the figures. LK and ME prepared the MGA^3 instrument for ASIA-AQ. LK, ME, PW and AR operated the instrument at GHGMon and ASIA-AQ and conducted the measurements. AF and MP contributed to the manuscript and discussion. OA provided the new v2 software for the MGA^3. GD, JD, YH and JM operated the DACOM and DLH instruments at ASIA-AQ and provided the respective data and also provided altitude above ground level data for the DC-8 at ASIA-AQ.

https://doi.org/10.5194/egusphere-2026-1686
Preprint. Discussion started: 10 April 2026

RB, CG, JDD and RP provided GPS-data, wind measurements, static pressure measurements, cabin pressure measurements and roll and pitch angle data from the DC-8 at ASIA-AQ. GL and JK provided the LGR-NH_3 measurements at ASIA-AQ. All authors contributed to the manuscript and the discussion.

Competing interests. The authors have no competing interests.

https://doi.org/10.5194/egusphere-2026-1686
Preprint. Discussion started: 10 April 2026

References

Behera, S. N., Sharma, M., Aneja, V. P., and Balasubramanian, R.: Ammonia in the atmosphere: a review on emission sources, atmospheric chemistry and deposition on terrestrial bodies, Environmental science and pollution research international, 20, 8092–8131, https://doi.org/10.1007/s11356-013-2051-9, 2013.

Capasso, F.: High-performance midinfrared quantum cascade lasers, Optical Engineering, 49, 111 102, https://doi.org/10.1117/1.3505844, 2010.

CCAC: Global Nitrous Oxide Assessment – Supplementary Information, https://www.ccacoalition.org/resources/global-nitrous-oxide-assessment, supplementary information to the Global Nitrous Oxide Assessment report; last accessed 8 September 2025, 2024.

Chadwick, D. R., Cardenas, L., Misselbrook, T. H., Smith, K. A., Rees, R. M., Watson, C. J., McGeough, K. L., Williams, J. R., Cloy, J. M., Thorman, R. E., and Dhanoa, M. S.: Optimizing chamber methods for measuring nitrous oxide emissions from plot–based agricultural experiments, European Journal of Soil Science, 65, 295–307, https://doi.org/10.1111/ejss.12117, 2014.

Crawford, J., Lefer, B., Zavaleta, J. R., Adachi, K., Apel, E., Bennett, J. R., Blake, D., Caulton, D., Dibb, J., Digangi, J. P., Diskin, G. S., Franchin, A., Gatebe, C. K., Hall, S., Huey, G., Jimenez, J.-L., Jordan, C., Kim, S., Lee, G., Lee, H., Lee, T., Lim, S., Miech, J., Min, K.-E., Moore, R., Roiger, A., Silverman, M., St. Clair, J., Wennberg, P., Wisthaler, A., Wolfe, G., Yum, S. S., and Zondlo: Airborne and Satellite Investigation of Asian Air Quality Campaign Data, https://doi.org/10.5067/SUBORBITAL/ASIA-AQ/DATA001, 2025.

Dacic, N., Plant, G., and Kort, E. A.: Airborne Measurements Reveal High Spatiotemporal Variation and the Heavy–Tail Characteristic of Nitrous Oxide Emissions in Iowa, Journal of geophysical research. Atmospheres : JGR, 129, https://doi.org/10.1029/2024JD041403, 2024.

Davidson, E. A. and Kanter, D.: Inventories and scenarios of nitrous oxide emissions, Environmental Research Letters, 9, 105 012, https://doi.org/10.1088/1748-9326/9/10/105012, 2014.

Del Grosso, S. J., Ogle, S. M., Nevison, C., Gurung, R., Parton, W. J., Wagner-Riddle, C., Smith, W., Winiwarter, W., Grant, B., Tenuta, M., Marx, E., Spencer, S., and Williams, S.: A gap in nitrous oxide emission reporting complicates long-term climate mitigation, Proceedings of the National Academy of Sciences of the United States of America, 119, e2200354 119, https://doi.org/10.1073/pnas.2200354119, 2022.

Diskin, G. S., Podolske, J. R., Sachse, G. W., and Slate, T. A.: Open-path airborne tunable diode laser hygrometer, in: Diode Lasers and Applications in Atmospheric Sensing, edited by Fried, A., SPIE Proceedings, p. 196, SPIE, https://doi.org/10.1117/12.453736, 2002.

Eckl, M., Roiger, A., Kostinek, J., Fiehn, A., Huntrieser, H., Knote, C., Barkley, Z. R., Ogle, S. M., Baier, B. C., Sweeney, C., and Davis, K. J.: Quantifying Nitrous Oxide Emissions in the U.S. Midwest: A Top–Down Study Using High Resolution Airborne In–Situ Observations, Geophysical Research Letters, 48, https://doi.org/10.1029/2020GL091266, 2021.

Gordon, I. E., Rothman, L. S., Hill, C., Kochanov, R. V., Tan, Y., Bernath, P. F., Birk, M., Boudon, V., Campargue, A., Chance, K. V., Drouin, B. J., Flaud, J.-M., Gamache, R. R., Hodges, J. T., Jacquemart, D., Perevalov, V. I., Perrin, A., Shine, K. P., Smith, M.-A., Tennyson, J., Toon, G. C., Tran, H., Tyuterev, V. G., Barbe, A., Császár, A. G., Devi, V. M., Furtenbacher, T., Harrison, J. J., Hartmann, J.-M., Jolly, A., Johnson, T. J., Karman, T., Kleiner, I., Kyuberis, A. A., Loos, J., Lyulin, O. M., Massie, S. T., Mikhailenko, S. N., Moazzen-Ahmadi, N., Müller, H., Naumenko, O. V., Nikitin, A. V., Polyansky, O. L., Rey, M., Rotger, M., Sharpe, S. W., Sung, K., Starikova, E., Tashkun, S. A., Auwera, J. V., Wagner, G., Wilzewski, J., Wcisło, P., Yu, S., and Zak, E. J.: The HITRAN2016 molecular spectroscopic database, Journal of Quantitative Spectroscopy and Radiative Transfer, 203, 3–69, https://doi.org/10.1016/j.jqsrt.2017.06.038, 2017.

https://doi.org/10.5194/egusphere-2026-1686
Preprint. Discussion started: 10 April 2026

Gordon, I. E., Rothman, L. S., Hargreaves, R. J., Hashemi, R., Karlovets, E. V., Skinner, F. M., Conway, E. K., Hill, C., Kochanov, R. V., Tan, Y., Wcisło, P., Finenko, A. A., Nelson, K., Bernath, P. F., Birk, M., Boudon, V., Campargue, A., Chance, K. V., Coustenis, A., Drouin, B. J., Flaud, J.-M., Gamache, R. R., Hodges, J. T., Jacquemart, D., Mlawer, E. J., Nikitin, A. V., Perevalov, V. I., Rotger, M., Tennyson, J., Toon, G. C., Tran, H., Tyuterev, V. G., Adkins, E. M., Baker, A., Barbe, A., Canè, E., Császár, A. G., Dudaryonok, A., Egorov, O., Fleisher, A. J., Fleurbaey, H., Foltynowicz, A., Furtenbacher, T., Harrison, J. J., Hartmann, J.-M., Horneman, V.-M., Huang, X., Karman, T., Karns, J., Kassi, S., Kleiner, I., Kofman, V., Kwabia-Tchana, F., Lavrentieva, N. N., Lee, T. J., Long, D. A., Lukashevskaya, A. A., Lyulin, O. M., Makhnev, V., Matt, W., Massie, S. T., Melosso, M., Mikhailenko, S. N., Mondelain, D., Müller, H., Naumenko, O. V., Perrin, A., Polyansky, O. L., Raddaoui, E., Raston, P. L., Reed, Z. D., Rey, M., Richard, C., Tóbiás, R., Sadiek, I., Schwenke, D. W., Starikova, E., Sung, K., Tamassia, F., Tashkun, S. A., Vander Auwera, J., Vasilenko, I. A., Vigasin, A. A., Villanueva, G. L., Vispoel, B., Wagner, G., Yachmenev, A., and Yurchenko, S. N.: The HITRAN2020 molecular spectroscopic database, Journal of Quantitative Spectroscopy and Radiative Transfer, 277, 107 949, https://doi.org/10.1016/j.jqsrt.2021.107949, 2022.

Gvakharia, A., Kort, E. A., Smith, M. L., and Conley, S.: Testing and evaluation of a new airborne system for continuous N 2 O, CO 2 , CO, and H 2 O measurements: the Frequent Calibration High-performance Airborne Observation System (FCHAOS), Atmospheric Measurement Techniques, 11, 6059–6074, https://doi.org/10.5194/amt-11-6059-2018, 2018.

Gvakharia, A., Kort, E. A., Smith, M. L., and Conley, S.: Evaluating Cropland N 2 O Emissions and Fertilizer Plant Greenhouse Gas Emissions With Airborne Observations, Journal of geophysical research. Atmospheres : JGR, 125, https://doi.org/10.1029/2020JD032815, 2020.

Hundt, P. M., Tuzson, B., Aseev, O., Liu, C., Scheidegger, P., Looser, H., Kapsalidis, F., Shahmohammadi, M., Faist, J., and Emmenegger, L.: Multi-species trace gas sensing with dual-wavelength QCLs, Applied Physics B, 124, https://doi.org/10.1007/s00340-018-6977-y, 2018.

Kanter, D. R., Ogle, S. M., and Winiwarter, W.: Building on Paris: integrating nitrous oxide mitigation into future climate policy, Current Opinion in Environmental Sustainability, 47, 7–12, https://doi.org/10.1016/j.cosust.2020.04.005, 2020.

Kaufmann, S., Voigt, C., Jurkat, T., Thornberry, T., Fahey, D. W., Gao, R.-S., Schlage, R., Schäuble, D., and Zöger, M.: The airborne mass spectrometer AIMS – Part 1: AIMS-H 2 O for UTLS water vapor measurements, Atmospheric Measurement Techniques, 9, 939–953, https://doi.org/10.5194/amt-9-939-2016, 2016.

Kiemle, C., Fix, A., Fruck, C., Ehret, G., and Wirth, M.: Design study for an airborne N 2 O lidar, Atmospheric Measurement Techniques, 17, 6569–6578, https://doi.org/10.5194/amt-17-6569-2024, 2024.

Kostinek, J., Roiger, A., Davis, K. J., Sweeney, C., DiGangi, J. P., Choi, Y., Baier, B., Hase, F., Groß, J., Eckl, M., Klausner, T., and Butz, A.: Adaptation and performance assessment of a quantum and interband cascade laser spectrometer for simultaneous airborne in situ observation of CH 4 , C 2 H 6 , CO 2 , CO and N 2 O, Atmospheric Measurement Techniques, 12, 1767–1783, https://doi.org/10.5194/amt-12-1767-2019, 2019.

Lebegue, B., Schmidt, M., Ramonet, M., Wastine, B., Yver Kwok, C., Laurent, O., Belviso, S., Guemri, A., Philippon, C., Smith, J., and Conil, S.: Comparison of nitrous oxide (N 2 O) analyzers for high-precision measurements of atmospheric mole fractions, Atmospheric Measurement Techniques, 9, 1221–1238, https://doi.org/10.5194/amt-9-1221-2016, 2016.

Li, J. S., Chen, W., and Fischer, H.: Quantum Cascade Laser Spectrometry Techniques: A New Trend in Atmospheric Chemistry, Applied Spectroscopy Reviews, 48, 523–559, https://doi.org/10.1080/05704928.2012.757232, 2013.

Lopez, M., Schmidt, M., Yver, C., Messager, C., Worthy, D., Kazan, V., Ramonet, M., Bousquet, P., and Ciais, P.: Seasonal variation of N 2 O emissions in France inferred from atmospheric N 2 O and 222 Rn measurements, Journal of Geophysical Research: Atmospheres, 117, https://doi.org/10.1029/2012JD017703, 2012.

https://doi.org/10.5194/egusphere-2026-1686
Preprint. Discussion started: 10 April 2026

MacFarling Meure, C., Etheridge, D., Trudinger, C., Steele, P., Langenfelds, R., van Ommen, T., Smith, A., and Elkins, J.: Law Dome CO 2 , CH 4 and N 2 O ice core records extended to 2000 years BP, Geophysical Research Letters, 33, https://doi.org/10.1029/2006GL026152, 2006.

Myhre, G., Shindell, D., Bréon, F.-M., Collins, W., Fuglestvedt, J., Huang, J., Koch, D., Lamarque, J.-F., Lee, D., Mendoza, B., Nakajima, T., Robock, A., Stephens, G., Takemura, T., and Zhang, H.: Anthropogenic and Natural Radiative Forcing, in: Climate Change 2013: The Physical Science Basis. Contribution of Working Group I to the Fifth Assessment Report of the Intergovernmental Panel on Climate Change, edited by Stocker, T. F., Qin, D., Plattner, G.-K., Tignor, M., Allen, S. K., Boschung, J., Nauels, A., Xia, Y., Bex, V., and Midgley, P. M., Cambridge University Press, Cambridge, United Kingdom and New York, NY, USA, 2013.

Pattey, E., Edwards, G. C., Desjardins, R. L., Pennock, D. J., Smith, W., Grant, B., and MacPherson, J. I.: Tools for quantifying N2O emissions from agroecosystems, Agricultural and Forest Meteorology, 142, 103–119, https://doi.org/10.1016/j.agrformet.2006.05.013, 2007.

Pitt, J. R., Le Breton, M., Allen, G., Percival, C. J., Gallagher, M. W., Bauguitte, S. J.-B., O'Shea, S. J., Muller, J. B. A., Zahniser, M. S., Pyle, J., and Palmer, P. I.: The development and evaluation of airborne in situ N 2 O and CH 4 sampling using a quantum cascade laser absorption spectrometer (QCLAS), Atmospheric Measurement Techniques, 9, 63–77, https://doi.org/10.5194/amt-9-63-2016, 2016.

Prather, M. J. and Wilson, C. P.: Projecting nitrous oxide over the 21st century, uncertainty related to stratospheric loss, Proceedings of the National Academy of Sciences of the United States of America, 123, e2524123 123, https://doi.org/10.1073/pnas.2524123123, 2026.

Prather, M. J., Hsu, J., DeLuca, N. M., Jackman, C. H., Oman, L. D., Douglass, A. R., Fleming, E. L., Strahan, S. E., Steenrod, S. D., Søvde, O. A., Isaksen, I. S. A., Froidevaux, L., and Funke, B.: Measuring and modeling the lifetime of nitrous oxide including its variability, Journal of geophysical research. Atmospheres : JGR, 120, 5693–5705, https://doi.org/10.1002/2015JD023267, 2015.

Prather, M. J., Froidevaux, L., and Livesey, N. J.: Observed changes in stratospheric circulation: decreasing lifetime of N 2 O, 2005–2021, Atmospheric Chemistry and Physics, 23, 843–849, https://doi.org/10.5194/acp-23-843-2023, 2023.

Rapson, T. D. and Dacres, H.: Analytical techniques for measuring nitrous oxide, TrAC Trends in Analytical Chemistry, 54, 65–74, https://doi.org/10.1016/j.trac.2013.11.004, 2014.

Ravishankara, A. R., Daniel, J. S., and Portmann, R. W.: Nitrous oxide (N2O): the dominant ozone-depleting substance emitted in the 21st century, Science (New York, N.Y.), 326, 123–125, https://doi.org/10.1126/science.1176985, 2009.

Reay, D. S., Davidson, E. A., Smith, K. A., Smith, P., Melillo, J. M., Dentener, F., and Crutzen, P. J.: Global agriculture and nitrous oxide emissions, Nature Climate Change, 2, 410–416, https://doi.org/10.1038/nclimate1458, 2012.

Rella, C. W., Chen, H., Andrews, A. E., Filges, A., Gerbig, C., Hatakka, J., Karion, A., Miles, N. L., Richardson, S. J., Steinbacher, M., Sweeney, C., Wastine, B., and Zellweger, C.: High accuracy measurements of dry mole fractions of carbon dioxide and methane in humid air, Atmospheric Measurement Techniques, 6, 837–860, https://doi.org/10.5194/amt-6-837-2013, 2013.

Rogelj, J. and Lamboll, R. D.: Substantial reductions in non-CO2 greenhouse gas emissions reductions implied by IPCC estimates of the remaining carbon budget, Communications Earth & Environment, 5, https://doi.org/10.1038/s43247-023-01168-8, 2024.

Saboya, E., Manning, A. J., Levy, P., Stanley, K. M., Pitt, J., Young, D., Say, D., Grant, A., Arnold, T., Rennick, C., Tomlinson, S. J., Carnell, E. J., Artioli, Y., Stavert, A., Spain, T. G., O'Doherty, S., Rigby, M., and Ganesan, A. L.: Combining Top–Down and Bottom–Up Approaches to Evaluate Recent Trends and Seasonal Patterns in UK N 2 O Emissions, Journal of geophysical research. Atmospheres : JGR, 129, https://doi.org/10.1029/2024JD040785, 2024.

Sachse, G. W., Hill, G. F., Wade, L. O., and Perry, M. G.: Fast–response, high–precision carbon monoxide sensor using a tunable diode laser absorption technique, Journal of Geophysical Research: Atmospheres, 92, 2071–2081, https://doi.org/10.1029/JD092iD02p02071, 1987.

https://doi.org/10.5194/egusphere-2026-1686
Preprint. Discussion started: 10 April 2026

Schiller, C. L., Bozem, H., Gurk, C., Parchatka, U., Königstedt, R., Harris, G. W., Lelieveld, J., and Fischer, H.: Applications of quantum cascade lasers for sensitive trace gas measurements of CO, CH4, N2O and HCHO, Applied Physics B, 92, 419–430, https://doi.org/10.1007/s00340-008-3125-0, 2008.

Scott, S. G., Bui, T. P., Chan, K. R., and Bowen, S. W.: The Meteorological Measurement System on the NASA ER-2 Aircraft, Journal of Atmospheric and Oceanic Technology, 7, 525–540, https://doi.org/10.1175/1520-0426(1990)007<0525:TMMSOT>2.0.CO;2, 1990.

Smith, K. A.: Changing views of nitrous oxide emissions from agricultural soil: key controlling processes and assessment at different spatial scales, European Journal of Soil Science, 68, 137–155, https://doi.org/10.1111/ejss.12409, 2017.

Thompson, R. L., Lassaletta, L., Patra, P. K., Wilson, C., Wells, K. C., Gressent, A., Koffi, E. N., Chipperfield, M. P., Winiwarter, W., Davidson, E. A., Tian, H., and Canadell, J. G.: Acceleration of global N2O emissions seen from two decades of atmospheric inversion, Nature Climate Change, 9, 993–998, https://doi.org/10.1038/s41558-019-0613-7, 2019.

Tian, H., Pan, N., Thompson, R. L., Canadell, J. G., Suntharalingam, P., Regnier, P., Davidson, E. A., Prather, M., Ciais, P., Muntean, M., Pan, S., Winiwarter, W., Zaehle, S., Zhou, F., Jackson, R. B., Bange, H. W., Berthet, S., Bian, Z., Bianchi, D., Bouwman, A. F., Buitenhuis, E. T., Dutton, G., Hu, M., Ito, A., Jain, A. K., Jeltsch-Thömmes, A., Joos, F., Kou-Giesbrecht, S., Krummel, P. B., Lan, X., Landolfi, A., Lauerwald, R., Li, Y., Lu, C., Maavara, T., Manizza, M., Millet, D. B., Mühle, J., Patra, P. K., Peters, G. P., Qin, X., Raymond, P., Resplandy, L., Rosentreter, J. A., Shi, H., Sun, Q., Tonina, D., Tubiello, F. N., van der Werf, G. R., Vuichard, N., Wang, J., Wells, K. C., Western, L. M., Wilson, C., Yang, J., Yao, Y., You, Y., and Zhu, Q.: Global nitrous oxide budget (1980–2020), Earth System Science Data, 16, 2543–2604, https://doi.org/10.5194/essd-16-2543-2024, 2024.

UNFCCC: Paris Climate Change Conference - November 2015: COP 21 Session, https://unfccc.int/documents/184656, last viewed: 04.09.2025, 2018.

Waldmann, P., Eckl, M., Knez, L., Gottschaldt, K.-D., Fiehn, A., Mallaun, C., Gałkowski, M., Kiemle, C., Hutjes, R., Röckmann, T., Chen, H., and Roiger, A.: Quantifying agricultural N 2 O and CH 4 emissions in the Netherlands using an airborne eddy covariance system, Atmospheric Measurement Techniques, 19, 185–210, https://doi.org/10.5194/amt-19-185-2026, 2026.

Werle, P., Mcke, R., and Slemr, F.: The limits of signal averaging in atmospheric trace-gas monitoring by tunable diode-laser absorption spectroscopy (TDLAS), Applied Physics B, 57, 131–139, https://doi.org/10.1007/BF00425997, 1993.

Xiang, B., Miller, S. M., Kort, E. A., Santoni, G. W., Daube, B. C., Commane, R., Angevine, W. M., Ryerson, T. B., Trainer, M. K., Andrews, A. E., Nehrkorn, T., Tian, H., and Wofsy, S. C.: Nitrous oxide (N 2 O) emissions from California based on 2010 CalNex airborne measurements, Journal of geophysical research. Atmospheres : JGR, 118, 2809–2820, https://doi.org/10.1002/jgrd.50189, 2013.